THE ASTROPHYSICAL JOURNAL, 414:676–694, 1993 September 10

THE EMBEDDED YOUNG STARS IN THE TAURUS-AURIGA MOLECULAR CLOUD. I. MODELS FOR SPECTRAL ENERGY DISTRIBUTIONS

SCOTT J. KENYON
Harvard-Smithsonian Center for Astrophysics, 60 Garden Street, Cambridge, MA 02138
NURIA CALVET[1]
Centro de Investigaciones de Astronomía, Apartado Postal 264, Mérida 5101-A, Venezuela
AND
LEE HARTMANN
Harvard-Smithsonian Center for Astrophysics, 60 Garden Street, Cambridge, MA 02138
Received 1993 February 8; accepted 1993 March 16

ABSTRACT

We describe radiative transfer calculations of infalling, dusty envelopes surrounding pre–main-sequence stars and use these models to derive physical properties for a sample of 21 heavily reddened young stars ("protostars") in the Taurus-Auriga molecular cloud. The density distributions needed to match the far-infrared peaks in the spectral energy distributions of these embedded sources suggest mass infall rates similar to those predicted for simple thermally supported clouds with temperatures ~ 10 K. Unless the dust opacities are badly in error, our models require substantial departures from spherical symmetry in the envelopes of all sources, as in Terebey, Shu, & Cassen's rotating infall solutions. These flattened envelopes may be produced by a combination of rotation and cavities excavated by bipolar flows. Terebey, Shu, & Cassen's models indicate a centrifugal radius of ~ 70 AU for many objects if rotation is the only important physical effect, and this radius is reasonably consistent with typical estimates for the sizes of circumstellar disks around T Tauri stars.

Subject headings: ISM: clouds — radiative transfer — stars: formation — stars: pre–main-sequence

1. INTRODUCTION

The standard picture of low-mass star formation predicts a nearly free-fall collapse of a dense molecular cloud core onto a central stellar object surrounded by a circumstellar disk (cf. Shu, Adams, & Lizano 1987). The molecular cloud is optically thick to short-wavelength radiation ($\lambda < 10$–30 μm) during the infall phase, so an extended dust photosphere emits most of the radiation at far-infrared (far-IR) wavelengths ($\lambda \sim 50$–100 μm). Various surveys using data collected by the *Infrared Astronomical Satellite* (*IRAS*) have identified a population of heavily reddened (and presumably very young) sources in nearby molecular clouds (e.g., Beichman et al. 1986; Meyers et al. 1987; Wilking, Lada, & Young 1989; Kenyon et al. (1990; Beichman, Boulanger, & Moshir 1992), and the spectral energy distributions of these objects agree with the basic predictions of the standard model (Adams & Shu 1986; Adams, Lada, & Shu 1987, hereafter ALS).

The spectral energy distributions of heavily embedded sources are determined mainly by the transfer of radiation through their dusty envelopes, so comparisons between observations and models can test the infall picture. Myers et al. (1987) pointed out that the extinctions to many embedded objects are too large to be explained in terms of the typical gas column densities in molecular cloud cores; the density must then rise sharply near the central source as predicted by the infall picture. ALS computed emergent fluxes for the Terebey, Shu, & Cassen (1984) rotationally flattened infall solution and showed that such models could account for the broad-band spectral energy distributions of several heavily reddened young objects using physically plausible input parameters. More recently, Butner et al. (1991) tested the standard picture in greater detail for L1551 IRS 5 using spatially resolved far-IR observations as additional constraints.

The general plausibility of the infall model seems established from detailed investigations of a few objects, but it is important to model a larger population of embedded sources. The overall results are then less sensitive to the particular circumstances of an individual source (binary companions, axial inclination, etc.), and a reasonably complete sample should allow us to address evolutionary questions. Several groups have searched the Taurus-Auriga cloud intensively for embedded sources, and the population of ~ 20 objects seems fairly complete for bolometric luminosities exceeding ~ 0.2 $L_\odot$ (Beichman et al. 1986; Myers et al. 1987; Kenyon et al. 1990; Beichman et al. 1992).

In this paper we present models of the Taurus-Auriga embedded sources to test the standard infall picture in more detail and to derive independent estimates of the envelope infall rates. The density of the infalling envelope—which is related to the mass infall rate—generally sets the wavelength of the far-IR peak of the spectral energy distribution; data for a complete sample of objects thus provide a good statistical estimate of the infall rate in a typical molecular cloud. Our results for the majority of Taurus sources are consistent with predicted infall rates if we adopt standard dust opacities. The observations often indicate more near-IR flux than is predicted by our calculations. This result probably requires substantial departures from spherical symmetry in the infalling envelope, and bipolar cavities formed by powerful outflows therefore may be required to explain the observations of many objects. This hypothesis will be explored in more detail in the second paper of this series (Kenyon et al. 1993, hereafter Paper II), which examines near-IR colors and images of the embedded objects.

[1] Also Grup d'Astrofísica de la Societat Catalana de Física, Institut d' Estudis Catalans.

We describe our observations in § 2, develop the model predictions in § 3, compare the models and observations in § 4, discuss our results in § 5, and conclude with a brief summary in § 6.

2. OBSERVATIONAL DATA

In this paper we define embedded sources as pre–main-sequence stars whose ratio of *IRAS* to bolometric luminosity is $L_{IRAS}/L_{bol} \gtrsim 0.8$. This definition includes all class I objects with steeply rising spectral energy distributions from 2 to 25–100 μm (ALS; see also Myers et al. 1987; Kenyon et al. 1990) but excludes optically visible T Tauri stars with large *IRAS* luminosities, such as DG Tau and T Tau (Strom et al. 1989; Adams, Emerson, & Fuller 1990). To this sample we added several pre–main-sequence stars—GV Tau, HK Tau, and Haro 6-13—that show two distinct peaks in their spectral energy distributions at 1–2 μm and at 10–60 μm. Leinert & Haas (1989) demonstrated that GV Tau is a binary system comprised of a classical T Tauri star with little or no reddening and a heavily embedded, class I source. HK Tau and Haro 6-13 may be binaries like GV Tau, so we include these objects in our sample for completeness.

For this sample of 22 objects, we collected published photometry covering wavelengths ranging from 0.55 μm to 3 mm. We restricted our compilation of optical and near-IR data to "standard" filters—V (0.55 μm), R_C (0.64 μm), R_J (0.70 μm), I_C (0.79 μm), I_J (0.90 μm), J (1.25 μm), H (1.65 μm), K (2.22 μm), L (3.5 μm), M (4.8 μm), N (10 μm), Q (20 μm)—and averaged data for each source to produce mean K-magnitudes and colors ($V-K$, $J-K$, $K-N$, etc) for the entire sample. Most embedded sources have only 2–3 near-IR measurements and at most 1–2 measurements at 10–20 μm. Multiple observations of a given source usually agree to within ± 0.20 mag, which seems excellent considering the extremely red colors of most objects and the variations in central wavelengths of the broad-band filters from one observatory to the next (see Bessell & Brett 1988). The near-IR measurements for the very cold embedded source 04368+2557 are very uncertain ($\pm$1–2 mag), because this object is very faint and diffuse on near-IR images (Tamura et al. 1991; Paper II). Several other sources—04108+2803B, 04239+2436, and GV Tau—show very large scatter ($\sim$0.4–0.5 mag at K with much smaller changes in near-IR colors) that probably cannot be caused by either calibration uncertainties or the use of different aperture sizes (see Paper II). These sources might be actual variable stars, because T Tauri stars in the cloud display similar fluctuations at K (Kenyon & Hartmann 1993).

We supplemented the 0.55–20 μm data with observations from *IRAS*, the Kuiper Airborne Observatory (KAO), and various grouped-based facilities. For the *IRAS* data, we averaged fluxes from the *IRAS* Point Source Catalog, Version 2 (1988, hereafter PSC2), the *IRAS* Serendipitous Survey Catalog (Kleinmann et al. 1986), and ADDSCAN fluxes derived from the *IRAS* survey data (Weaver & Jones 1992; Kenyon et al. 1990). The average fluxes usually differed from PSC2 fluxes by less than 10%–20%, except in those few cases where ADDSCANS improved the individual fluxes of two sources separated by $\sim$30″–120″. We converted the magnitudes and colors into fluxes using standard calibrations (Bessell & Brett 1988; Rieke, Lebofsky, & Low 1985) and list the average fluxes and original references for our sample in Tables 1A–1D. The first set of data in each table corresponds to ground-based measurements in the "standard" broad-band filters and the *IRAS* fluxes, while the second set includes far-IR and submillimeter fluxes. The final row in each table lists the bolometric luminosity for each source, which we estimated in the three-step process. First, we derived the *IRAS* (7–135 μm) luminosity as described by Emerson (1988). We then integrated the data from the shortest wavelength measurement available (usually 1.25 μm) to 7 μm using logarithmic interpolation to construct a 7 μm flux and a trapezoidal integration routine. Finally, we logarithmically interpolated the 100–800 μm data to 135 μm and integrated the fluxes out to the longest wavelength measurement available (usually 1 mm). The bolometric flux is then the sum of these three integrations; we adopt a distance of 140 pc to convert this result into the bolometric luminosity.

3. MODELS

3.1. *Density Distributions*

We adopt the Terebey, Shu, & Cassen (1984, hereafter TSC; see also Ulrich 1976 and Cassen & Moosman 1981) solution for a collapsing protostellar cloud. In this model, the initial cloud rotates uniformly and has a radial density distribution approaching that of a singular isothermal sphere, $\rho(r) \propto r^{-2}$. Collapse begins first near the center. Information about the collapse propagates outward at the sound speed a and material outside a radius $r_s = at$ remains in hydrostatic equilibrium after a time t. Inside this radius, the infall velocity approaches free fall, $v \propto r^{-1/2}$; the density distribution converges toward $\rho \propto r^{-3/2}$, because the mass infall rate, $\dot{M}_i$, is constant. The angular momentum of the infalling gas becomes important in the vicinity of the centrifugal radius, R_c, and material then falls onto a circumstellar disk rather than radially onto the central object.

To calculate the radiative equilibrium temperature in the cloud, we use the angle-averaged density of TSC's inner solution (see Adams & Shu 1986):

$$\rho(r) = CA(u)r^{-3/2} , \quad (1)$$

where $u = r/R_c$ and R_c is the centrifugal radius. $A(u)$ is given by equation (10b) in Adams & Shu (1986). For $u \gg 1$, $A(u) \rightarrow 1$; as $u \rightarrow 0$, $A(u) \propto r$ and $\rho(r) \propto r^{-1/2}$. The parameter C is given by

$$C = \frac{\dot{M}_i}{4\pi(2GM_*)^{1/2}} , \quad (2)$$

where $\dot{M}_i$ and M_* are the mass infall rate and the stellar mass, respectively. We ignore the outer, static parts of the cloud, $r > r_s$, still in hydrostatic equilibrium.

Although we solve for the radiative equilibrium temperature using a spherically symmetric density distribution, we employ TSC's flattened, axially symmetric density distribution to derive the emergent flux distribution of the cloud. This approach differs from the Adams & Shu (1986; see also ALS) models, which use the exact TSC density distribution to compute the attenuated energy distribution of the central star-disk system but employ the spherically average density (eq. [1]) to calculate the envelope emission. Thus, the ALS model spectral energy distributions vary much less with inclination than do ours (see below).

3.2. *Radiative Equilibrium Methods*

We assume that the system consists of a central stellar source, with bolometric luminosity L, surrounded by a spherically symmetric envelope, with inner radius r_{in} and outer

TABLE 1

OBSERVED FLUXES (λF_λ in ergs cm^{-2} s^{-1}) FOR TAURUS-AURIGA EMBEDDED SOURCES

A.

λ (μm)	04016+2610	04108+2803B	04166+2706	04169+2702	04181+2655	04181+2654B
0.55	−12.88	...	...	...	...	...
0.64	−12.54	...	...	...	...	
0.79	−12.19	...	...	...	...	...
1.22	−10.87	−11.92	...	−12.17	−11.67	−12.66
1.63	−10.40	−11.03	−11.36	−11.26	−10.89	−11.19
2.19	−9.80	−10.51	−10.68	−10.55	−10.34	−10.39
3.45	−9.40	−10.37	...	−10.23	...	...
4.75	−8.89	−9.97	...	...	...	...
10.6	−9.14	−9.77	...	−9.84	...	...
12.0	−9.02	−9.72	−10.76	−9.90	−9.85	−10.05
21.0	−8.82	−9.43	...	...	...	...
25.0	−8.71	−9.36	−10.16	−9.38	−9.69	−9.93
60.0	−8.62	−9.42	−9.57	−9.25	−9.73	−9.83
100.0	−8.73	−9.49	−9.55	−9.29	−9.51	−9.82
100.0	−8.78	...	...	...	...	...
160.0	−9.06	...	...	...	...	...
350.0	−10.39	...	...	...	...	
450.0	10.66	−10.92	...	...	...	
800.0	−11.93	−11.48	−11.61	−11.56	−12.96	−13.13
1100.0	−11.84	−12.62	−12.09	−12.12	...	...
log L	+0.57	−0.20	−0.51	−0.12	−0.42	−0.59

B.

λ (μm)	04181+2654A	04239+2436	04248+2612	GV Tau B	04264+2433	L1551 IRS 5
1.22	−11.70	−11.60	−10.52	...	−10.87	−10.66
1.63	−10.79	−10.86	−10.29	−10.31	−10.54	−10.14
2.19	−10.25	−10.24	−10.32	−9.97	−10.50	−9.77
3.45	−10.21	−9.70	−10.65	−9.26	−10.78	−9.47
4.75	...	...	...	−9.03	...	−9.17
10.6	...	...	−10.19	...	...	−8.88
12.0	−10.05	−9.37	−10.40	−8.44	−10.01	−8.61
21.0	...	−9.20	−9.91	...	...	−8.50
25.0	−9.93	−9.08	−9.81	−8.33	−9.45	−7.89
60.0	−9.83	−9.12	−9.62	−8.53	−9.58	−7.75
100.0	−9.82	−9.29	−9.53	−8.83	−10.32	−7.86
25.0	...	...	...	...	...	−8.12
40.0	...	...	...	...	...	−7.82
47.0	...	...	−9.76	...	...	−7.76
52.0	...	...	−9.73	−8.75	...	−7.69
65.0	...	...	−9.92	...	...	...
85.0	...	...	...	...	...	−7.58
95.0	...	...	−9.82	...	...	−7.93
100.0	...	...	−9.82	−9.16	...	−7.85
150.0	...	...	...	...	...	−8.05
377.0	...	...	...	...	...	−9.07
600.0	...	...	...	−11.29	...	...
800.0	...	−11.06	−12.10	−11.76	...	...
811.0	...	...	...	...	...	−10.26
11.00.0	...	−12.68	−12.56	−12.52	...	...
3000.0	...	...	...	...	...	−12.89
log L	−0.60	+0.09	−0.45	+0.77	−0.44	+1.34

TABLE 1—*Continued*

C.

λ (μm)	HK Tau	Haro 6-13	04295+2251	04302+2247	04325+2402	04361+2547
0.36	−12.27	...	...	...	...	...
0.44	−11.65	...	...	...	...	...
0.55	−11.04	−11.78	...	...	...	...
0.64	−10.63	...	...	...	...	...
0.79	−10.17	...	...	...	...	...
1.22	−9.58	−9.64	−10.87	−11.10	...	−11.85
1.63	−9.38	−9.28	−10.18	−10.67	−10.94	−10.88
2.19	−9.43	−9.12	−9.89	−10.49	−10.48	−10.28
3.45	−9.71	−9.17	−9.84	−10.75	...	−10.08
4.75	−9.89	−9.27	...	...	...	−9.85
10.6	−10.21	−9.65	−9.78	...	...	−9.57
12.0	−10.13	−9.56	−9.81	...	...	−9.35
21.0	−10.03	−9.37	...	...	...	...
25.0	−9.93	−9.31	−9.65	−10.33	−9.63	−8.64
60.0	−9.88	−9.42	−9.76	−9.48	−9.19	−8.66
100.0	−9.76	−9.52	−9.61	−9.55	−9.18	−8.93
47.0	...	−9.63	...	...	...	...
95.0	...	−9.71	...	...	...	...
450.0	−10.95	...	...	...	...	...
600.0	...	−11.51	...	...	...	...
800.0	−12.10	−11.76	...	...	...	...
1100.0	−12.52	−12.22	...	...	...	...
1300.0	−13.02	−12.54	...	...	...	...
log *L*	−0.13	+0.12	−0.36	−0.48	−0.14	+0.46

D.

λ (μm)	04365+2535	04368+2557	04381+2540	04489+3042
1.22	−12.30	−11.36	−11.90	−10.92
1.63	−11.06	−11.19	−11.46	−10.36
2.19	−10.28	−10.88	−10.86	−10.11
3.45	−9.91	...	−10.39	−10.20
4.75	−9.30	...	...	...
10.6	−9.76	...	−10.23	−10.07
12.0	−9.52	−10.60	−9.99	−9.98
21.0	−9.14	...	−10.55	...
25.0	−8.96	−10.08	−9.48	−9.78
60.0	−8.74	−9.06	−9.28	−9.91
100.0	−8.89	−8.67	−9.35	−9.75
160.0	...	−8.89	...	...
350.0	...	−9.99	...	...
450.0	...	−10.67	...	...
800.0	...	−11.73	...	...
log *L*	+0.35	+0.13	−0.18	−0.53

REFERENCES.—Barsony & Kenyon (1992; submillimeter photometry); Beckwith & Sargent (1991; 1 mm photometry); Beichman & Harris (1981; 5–20 μm photometry); Benson, Myers, & Wright (1984; *JHKLM* photometry); Chini et al. (1984; 1 mm photometry); Cohen, Harvey, & Schwartz (1985; far-IR photometry); Cohen & Kuhi (1979; *JHKL* photometry); Cohen & Schwartz (1983; 1–20 μm photometry); Cohen et al. (1984; far-IR photometry); Elias (1978; *JHKLN* photometry); Harvey, Thronson, & Gatley (1979; far-IR photometry); Kenyon et al. (1990; *JHKL* photometry + *IRAS* ADDSCANS); Kim (1990; *JHK* photometry); Ladd et al. (1991a, far-IR + submillimeter photometry); Leinert & Haas (1989; *HKLM* photometry); Moneti & Zinnecker (1991; *JK* photometry); Myers et al. (1987; 0.5–20 μm photometry); Price & Murdock (1983; 4–20 μm photometry); Price, Murdock, & Shivanandan (1983; 4–20 μm photometry); Rydgren & Vrba (1983; *UVBRIJHKL* photometry); Strom, Strom, & Vrba (1976; *JHKLM* photometry); Tamura et al. (1991; *K* images); Tamura & Sato (1989; *JHK* polarimetry); Terebey et al. (1990; 2–20 μm photometry); Weintraub, Sandell, & Duncan (1989; submillimeter photometry); Paper II (1993; *JHK* images).

radius $r_{out}(<r_s)$. The inner radius of the envelope is set by the dust destruction radius, which we assume occurs at a temperature of 1500 K. The actual dust destruction temperature depends on the composition and the density, and generally lies between 1000 and 2000 K (cf. Stahler, Shu, & Taam 1981; Wolfire & Cassinelli 1987). Our model spectral energy distributions are not very sensitive to the temperature at $r = r_{in}$. We ignore the interaction of radiation from the central object with envelope matter located inside this radius, because molecular opacities are several orders of magnitude lower than the dust opacity. We adopt $r_{out} = 3000$ AU, which corresponds to an angular size of $\sim 20''$ at the distance to the Taurus dark cloud ($d = 140$ pc). Our choice of r_{out} is appropriate for collapsing clouds with sound speeds, $a \sim 0.1$–0.2 km s^{-1}, and ages, $t \sim 10^5$ yr, close to those previously estimated for the Taurus-Auriga embedded sources (ALS; Myers et al. 1987; Benson & Myers 1989; Kenyon et al. 1990). Our model spectral energy distributions are sensitive to r_{out} only for $\lambda \gtrsim 100$ μm, and few data at these wavelengths are available for our embedded sample (Table 1). Several sources have far-IR angular sizes exceeding our outer radius limit (e.g., Ladd et al. 1991b), while L1551 IRS 5 appears smaller than this limit (Butner et al. 1991). The vast majority of embedded objects have no spatial information at far-IR wavelengths, so we ignore material outside $\sim 20''$ in this initial study.

Our calculation for the radiative equilibrium temperature in the angle-averaged density distribution employs the Unsöld-Lucy method, generalized to spherical symmetry (Cassinelli & Hartmann 1975), and solves the radial transfer equation for the mean intensity and flux using variable Eddington factors (Mihalas 1978). We estimate the Eddington factors from a ray-by-ray solution using the source function from the previous iteration, which has given reliable convergence for similar problems (Hummer & Rybicki 1971; Cassinelli & Hummer 1971). The source function assumes coherent and isotropic scattering. Silicate and graphite grains are the main opacity sources in the envelope, and we adopt optical constants and abundances from Draine & Lee (1984) and Draine (1987).

We use the *angle-averaged* density distribution to construct the spherically symmetric source function, $S_\nu = \sigma_\nu J_\nu + (1 - \sigma_\nu)B_\nu$, where σ_ν is the albedo and B_ν is the Planck function. Scattering increases the flux at short wavelengths, $\lambda \lesssim 3$ μm. We then derive the emergent flux from the envelope using S_ν for the source function and the *angle-dependent* density, $\rho(r, \theta)$, for the opacity. This envelope flux depends on the inclination, because the optical depth is much smaller along the rotational pole than at the equator, so the inclination is (unfortunately) an important parameter of the models. Our approximate approach is valid as long as energy is roughly conserved; we find that the total luminosity emerging from the envelope, $\int 4\pi H_{\nu,i}(r_{out}) r_{out}^2 \, d\nu$, usually agrees with the stellar luminosity to within 10%. In general, the source function should account for departures from spherical symmetry, but more detailed calculations suggest that these departures are not too important (Efstathiou & Rowan-Robinson 1990; see also § 5.1).

Our assumption of a central spherically symmetric source is not valid if a disk emits most of the system luminosity. The illumination of the inner envelope will then be angle-dependent, because disks radiate most of their energy along the rotational axis. We expect that the resultant temperature distribution in the envelope will also be angle-dependent, which we cannot investigate with the present treatment.

Aside from our use of the angle-dependent density to derive the emitted flux, our approach differs from that of ALS in two other respects. First, we include isotropic scattering by dust grains, which increases the near-IR emission relative to that of the purely absorptive grains assumed in the ALS calculations. However, we still cannot match the observed level of near-IR emission in these sources (see below); Paper II will consider a better treatment of scattering that *can* account for the near-IR fluxes. Second, we consider the source luminosity, L, as a free parameter in the models and do not attempt to set L according to the infall rate (as in the stellar birth-line models of Stahler 1988). This approach allows the disk accretion rate to differ from the infall rate and will be discussed in § 5.2.

3.3. *Model Results*

3.3.1. *Power Law (Spherically Symmetric) Density Distributions*

We begin with a grid of spherically symmetric models having a simple power-law density distribution, $\rho(r) = Cr^{-3/2}$, which is equivalent to equation (1) for very small R_c. The constant C sets the scale of the density distribution; we prefer to define these models in terms of ρ_1, the density at $r = 1$ AU in the limit that $R_c \rightarrow 0$. We can relate this parameter to the mass infall rate and central mass as (see eq. [2])

$$\rho_1 = 5.3 \times 10^{-14} \left(\frac{\dot{M}_i}{10^{-5} \, M_\odot \, \mathrm{yr}^{-1}} \right) \left(\frac{M_*}{1 \, M_\odot} \right)^{-1/2} g \, \mathrm{cm}^{-3} . \quad (3)$$

The total luminosity of the central object is the other parameter that defines a model. The temperature distribution in the envelope is not very sensitive to the spectral energy distribution of the central light source, because the optical depth at wavelengths $\lesssim 3$ μm is so large that the innermost portions of the envelope quickly redistribute this radiation to longer wavelengths.

Figure 1 shows temperature profiles for three densities, $\rho_1 = 10^{-14}$, 10^{-13}, and 10^{-12} g cm^{-3}, and four stellar luminosities, $L = 10^{32}$, 10^{33}, 10^{34}, and 10^{35} ergs s^{-1}. The temperature at a given radius increases with the luminosity of the central source; thus, the dust destruction radius increases from a few stellar radii for $L \approx 10^{32}$ ergs s^{-1} to ~ 1 AU for $L \approx 10^{35}$ ergs s^{-1}. The temperature distributions display two different radial gradients, $T(r) \propto r^{-\alpha}$, with $\alpha \approx 0.7$ in an optically thick inner region ($T \sim 100$–1500 K) and $\alpha \lesssim 0.3$ in an optically thin outer region ($T \lesssim 100$ K). Most of the energy in the inner region is absorbed and emitted at $\lambda < 30$ μm, where the radial optical depth through the envelope ranges from $\tau_{30\,\mu m} = 4$ for $\log \rho_1 = -14$ to $\tau_{30\,\mu m} = 150$ for $\log \rho_1 = -12$ and $\log L = 33$. The opacity law drops steeply at longer wavelengths (which correspond to lower temperatures); the outer parts of the envelope then become optically thin and the temperature gradient becomes shallower. We describe the reasons for this behavior in the Appendix.

Figure 2 shows spectral energy distributions for the spherically symmetric models. We draw several general conclusions from these models (see also Adams & Shu 1985, 1986, and references therein): (1) the peak of the energy distribution shifts to longer wavelengths as the envelope density increases; (2) the peak of the energy distribution also shifts to longer wavelengths as the luminosity decreases; (3) the spectral energy distributions become broader as the density decreases; and (4) the depth of the silicate features decreases with increasing luminosity.

In the Appendix we derive a simple scaling relation for the peak wavelength of the spectral energy distribution that

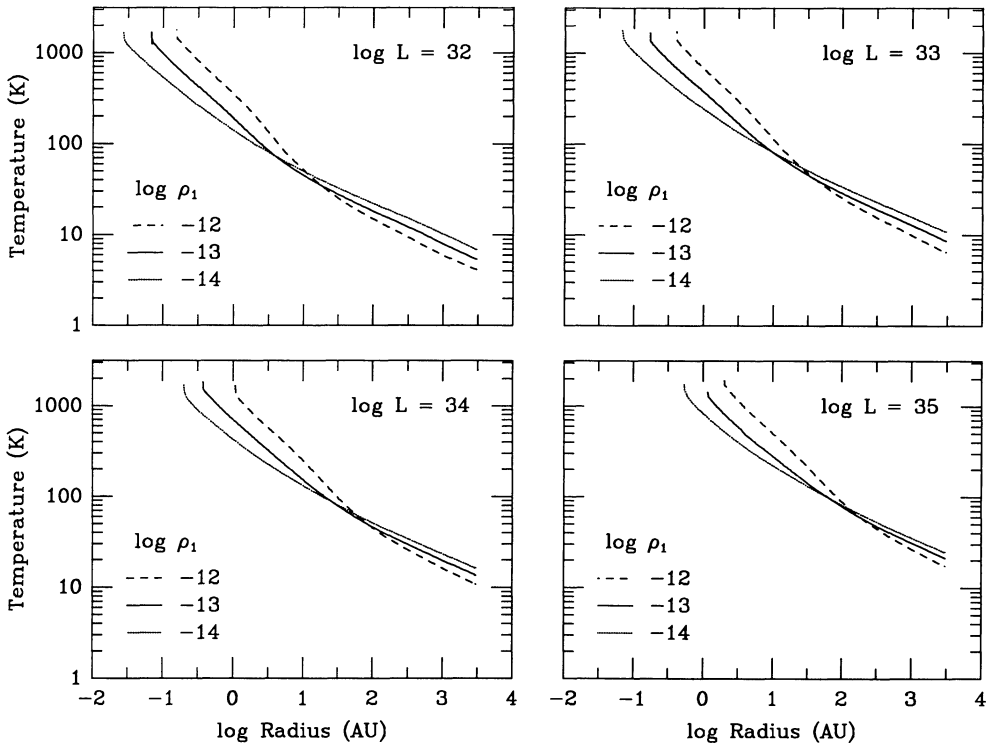

FIG. 1.—Radial temperature distributions for spherically symmetric infalling envelope models. Each panel plots the temperature for three different density distributions for the central source luminosity indicated in the upper right-hand corner of the panel.

explains properties 1 and 2:

$$\lambda_m \approx 60\left(\frac{L}{10^{33}\ \mathrm{ergs\ s^{-1}}}\right)^{-1/12}\left(\frac{\rho_1}{10^{-13}\ \mathrm{g\ cm^{-3}}}\right)^{1/3}\ \mu\mathrm{m}\ . \quad (4)$$

If we adopt a "standard" infall rate for Taurus-Auriga ($\dot{M}_i \sim$ a few times $10^{-6}\ M_\odot\ \mathrm{yr}^{-1}$ [ALS]) then $\rho_1 \sim 2 \times 10^{-14}\ \mathrm{g\ cm^{-3}}$ for $M_* \sim 0.5\ M_\odot$. The peak of the spectral energy distribution is then $\lambda_{\max} \approx 40$–$80\ \mu$m for log $L = 35$–32, which roughly corresponds to the observed range in L among the Taurus sources.

Properties 3 and 4 can be understood qualitatively in terms of the envelope opacity. Figure 3 shows the radius in the envelope where the radial optical depth, $\tau_\lambda(r)$, equals unity for log $L = 33$ and log $\rho_1 = -12$, -13, and -14. This radius increases as the wavelength decreases and the dust opacity increases. The entire envelope becomes optically thin at large wavelengths, and the $\tau = 1$ radius coincides with the inner radius of the envelope in the figure (even though the value of the total optical depth in less than unity). The temperature at the radius gives an indication of the highest temperature region that can be detected at a given wavelength, which is related to the emergent flux.

Property 3 arises because the wavelength dependence of the dust opacity changes between the mid-IR and the far-IR. At high densities, the peak of the spectral energy distribution occurs at long wavelengths where the opacity steeply increases with decreasing wavelength. Light from the hot inner regions is quickly absorbed by the overlying envelope. At low densities, the peak of the spectral energy distribution occurs near ~ 30 μm, where the dust opacity is relatively flat as a function of wavelength; therefore, light for the hot interior regions of the envelope is proportionately less extinguished by the overlying material, and the spectral energy distribution becomes flatter.

The silicate features at wavelengths of ~ 10 and 18 μm form at relatively large radii, because the opacity increases substantially at these wavelengths (Fig. 3). The outer envelope is very cold in low-luminosity cases, so the peak of the local Planck function moves to much longer wavelengths and the emergent intensity at 10–20 μm is very low. The outer envelope is much hotter at high luminosities, so the flux in the silicate features increases significantly (property 4).

3.3.2. *Non–Spherically Symmetric Density Distributions*

We next consider models with $R_c \gg R_*$. As mentioned in § 3.2, we calculate the temperature distribution with the average density, equation (1), for a central source of luminosity L and then determine the emergent flux from the actual axisymmetric density distribution. Thus, the emergent flux depends on the inclination angle i.

We begin with a discussion of models having log $L = 33$ to illustrate the effects of R_c on the spectral energy distribution. Figure 4 shows model fluxes for log $\rho_1 = -14$, -13, and -12, and $R_c = 70$ AU (for the two lower density cases) or 300 AU (for the highest density case) at several inclination angles. First, the breadth of the spectral energy distribution varies dramatically with inclination; in contrast, the ALS models change very little with inclination except at optical and millimeter wavelengths. In addition, the spectral energy distributions become significantly broader compared with the spherical case (Fig. 2) as ρ_1 decreases for $R_c > 0$. Figure 5 shows the reason for this behavior. The left-hand panel compares the radial density distribution of the spherically symmetric case to the angle-dependent density for several inclination angles, $\theta = 10°$,

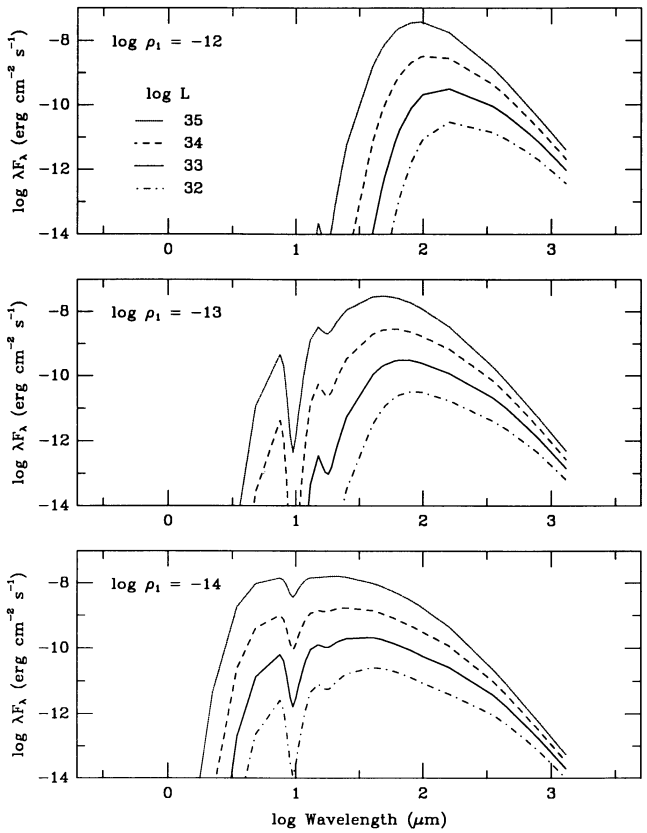

FIG. 2.—Emergent spectral energy distributions for spherically symmetric infalling envelope models. Each panel plots the flux distribution for four different central source luminosities for the characteristic density indicated in the upper left-hand corner of the panel.

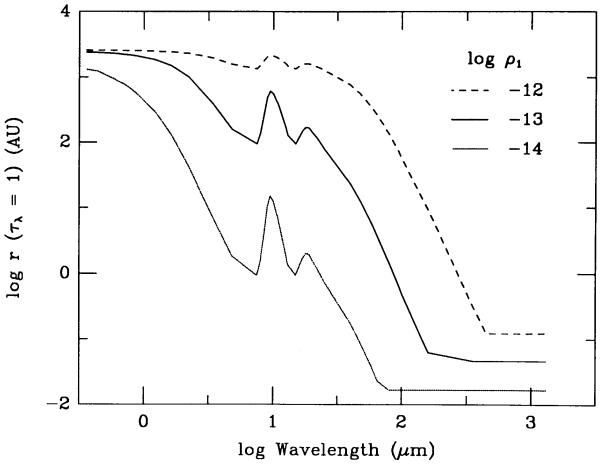

FIG. 3.—Photospheric radii as a function of wavelength for spherically symmetric infalling envelope models. The radius where the radial optical depth equals unity is a strong function of wavelength. The clouds are optically thin at long wavelengths and extremely opaque at short wavelengths; at a given wavelength, the radius for $\tau = 1$ decreases as the density decreases. Silicate absorption causes the prominent peak in the plots at 10 μm.

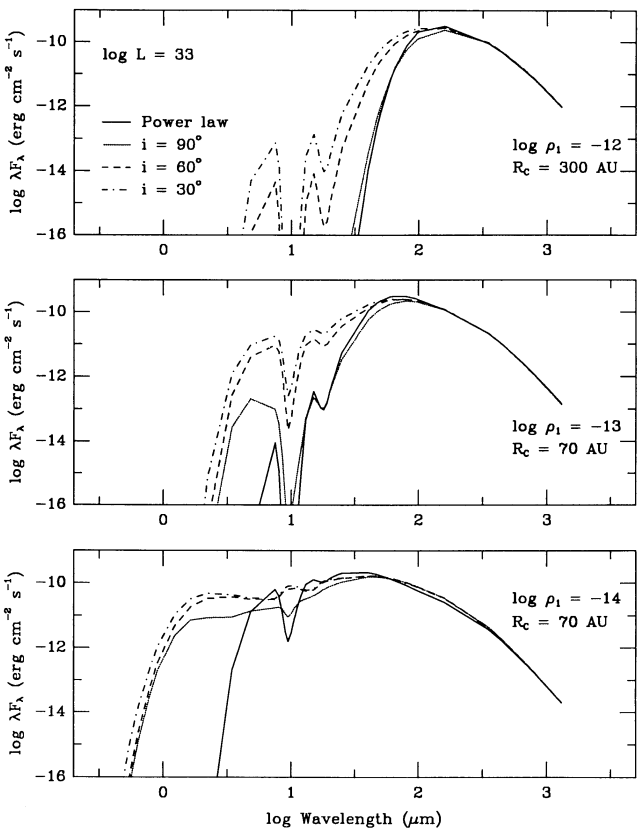

FIG. 4.—Emergent spectral energy distributions for models with flattened density distributions viewed at different inclination angles i. The central source luminosity for each model is 10^{33} ergs s^{-1}. *Top*: comparison of the spherically symmetric model ("power law;" *solid curve*) with models having large infall rates, log $\rho_1 = -12$, and centrifugal radii $R_c = 300$ AU, for inclinations $i = 30°$ (*dot-dash curve*), 60° (*dashed curve*), and 90° (*dotted curve*). *Middle*: as in top panel, but for log $\rho_1 = -13$ and $R_c = 70$ AU. *Bottom*: as in top panel, but for log $\rho_1 = -14$ and $R_c = 70$ AU. The spectral energy distributions become broader—and silicate absorption at 10 μm becomes shallower—as ρ_1 and R_c decrease.

30°, 60°, and 80°, assuming log $L = 33$, log $\rho_1 = -13$, and $R_c = 70$ AU. For $r \leq R_c$, the density drops significantly below the power-law distribution (the density law actually has a singularity at $r = R_c$ for $\theta = 90°$, which we have avoided by forcing the streamline to touch the x-y plane at this point). This decrease in density implies that the optical depth decreases and the envelope becomes optically thin at all wavelengths except those for which $\tau_\lambda \gtrsim 1$ at $r > R_c$.

The right-hand of Figure 5 shows how R_c changes $r(\tau_\lambda) = 1$ for a model with log $L = 33$, log $\rho_1 = -13$, and $R_c = 70$ AU. The optical depth increases very little at any wavelength for $r < R_c$, because the density gradient is so shallow. Thus, the envelope only becomes optically thick at wavelengths where the opacity is high enough that τ_λ exceeds unity at R_c. The angle dependence of the density makes the envelope thinner as inclination decreases. In particular, the envelope becomes so optically thin at low inclinations that the silicate features turn into emission at low infall rates (e.g., log $\rho_1 = -14$). At high inclinations, the axisymmetric envelope is denser than the angle-averaged case, and the silicate features appear in absorption.

The small optical depth in the envelope for large R_c implies that more direct (near-IR) light from the central object escapes the envelope compared with the power-law density cases. Thus, the emergent spectral energy distribution depends more upon the exact spectrum of the central object (the spectral energy distributions shown in Fig. 4 assume a central star of

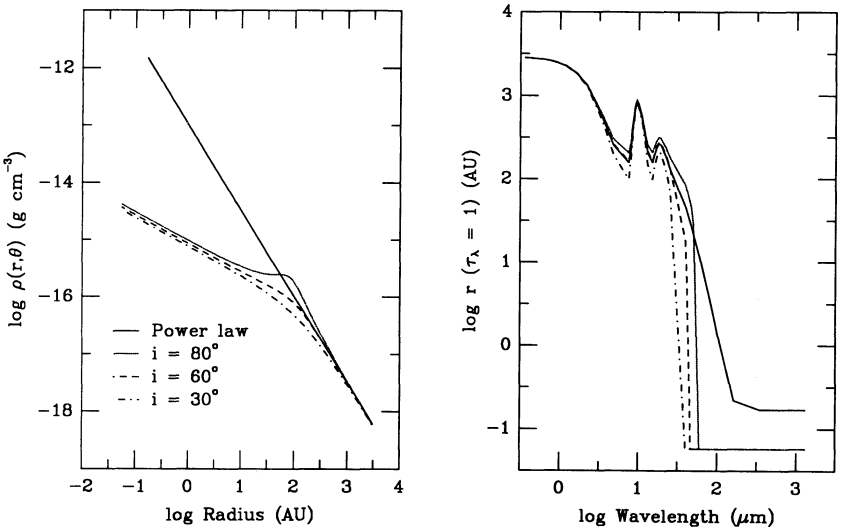

FIG. 5.—Density and radial optical depth distributions for flattened model envelopes with $R_c = 70$ AU. *Left*: Radial density distributions for three inclination angles compared with the spherically symmetric distribution (*solid line*). The angle-dependent density distributions closely follow the spherically symmetric case for $r \gg R_c$ and are considerably flatter than the spherical case for $r < R_c$. *Right*: Photospheric radius as a function of wavelength for three inclination angles compared with the spherically symmetric distribution (*solid line*). The cloud is very opaque at wavelengths below a few microns, and the shallower density distribution inside R_c does not change the emitted spectrum. An outside observer can see farther into the cloud as the wavelength increases, so the shallower density gradient becomes more obvious.

$T_{\rm eff} = 3500$ K). To investigate this feature of the infall solution, we tried models in which the central star is surrounded by a disk that contributes a fraction of the total luminosity L. We derive the source function assuming the spherically averaged density and a central object with a spectral energy distribution equivalent to that of a star with luminosity βL and a disk with luminosity $(1 - \beta)L$. As discussed in § 3.2, disks radiate more energy out along the rotational axis than out through the equatorial regions, so our basic assumption of spherical symmetry breaks down. However, we find that our models still conserve the total system luminosity to within 10% for $\beta \geq \frac{1}{2}$.

We assume that the disk's radial temperature distribution is $T_d(r) = T_{d0}(r/R_*)^{-3/4}$, so

$$T_{d0} = [(1 - \beta)(L/4\pi\sigma_R R_*^2)(1 - R_*/R_c)]^{1/4}$$

when the maximum disk radius is R_c and its minimum radius is R_*. We further assume the disk to be optically thick up to a radius $R_{\rm thick} \leq R_c$. Thus, disk material at $r \leq R_{\rm thick}$ contributes a flux $B_\lambda[T_d(r)]e^{-\tau_\lambda}$, where τ_λ is the optical depth along a ray from the observer through the envelope that intersects the disk.

Figure 6 shows emergent fluxes for $\log L = 33$, $\log \rho_1 = -14$, and $R_c = 70$ AU; we consider a disk with $\beta = \frac{1}{2}$ and $R_{\rm thick} = R_c$ (*top panel*) or $R_{\rm thick} = 10$ AU (*bottom panel*). For comparison, dashed lines plot model fluxes when the central object is just a star with $T_{\rm eff} = 3500$ K. The disk introduces several new features in the energy distributions. First, the disk lowers the peak far-IR flux, because the envelope on the far side of the optically thick part of the disk cannot contribute to the flux. This feature obviously becomes less important if most of the disk is optically thin, and becomes more important as a larger fraction of the disk becomes opaque. Second, a disk increases the near-IR flux, because the envelope is not opaque enough to absorb disk light as it passes through the cloud. Third, radiation from material in the optically thick outer disk ($r \sim 20$–70 AU) increases the flux at millimeter wavelengths, because the contribution of the optically thin, dusty envelope at those wavelengths is small for our assumed maximum envelope radius of 3000 AU. Finally, the disk contribution to the spectral energy distribution decreases as the inclination increases.

We also examined cases with disks inside higher density envelopes. Disk radiation is less visible as ρ_1 increases—and is essentially invisible for $\log \rho_1 \gtrsim -13$—because the envelope becomes completely opaque at near-IR and mid-IR wave-

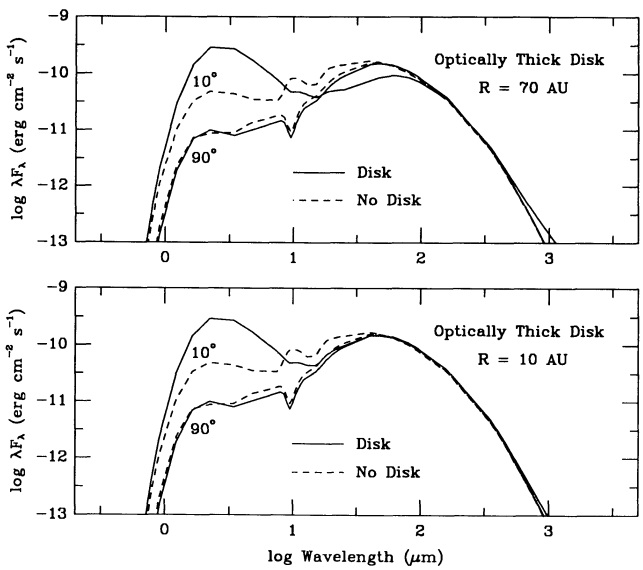

FIG. 6.—Comparison of model envelopes with and without radiation from an optically thick circumstellar disk. *Top*: dashed lines plot fluxes for envelope models with $\log L = 33$, $\log \rho_1 = -14$, and $R_c = 70$ AU at two inclination angles. The solid lines plot fluxes for the same envelope models with extra radiation from a large optically thick disk, $R_{\rm thick} = R_c$, with luminosity equal to the stellar luminosity. The total luminosity of the star + disk equals the luminosity of the central source in the envelope-only model. *Bottom*: as in top panel, for a disk with $R_{\rm thick} = 10$ AU.

lengths. The disk still contributes at millimeter wavelengths because our envelopes do not emit much radiation beyond ~ 1 mm.

4. COMPARISON OF MODELS WITH OBSERVATIONS

We next proceed to estimate parameters for the embedded sources in Taurus-Auriga by comparing the observed spectral energy distributions with our model grid. There clearly are uncertainties in these models, such as the importance of departures from spherical symmetry on the temperature distribution, scattered light at short wavelengths, the likely presence of companion stars, etc. By determining results for the entire ensemble of known embedded sources in Taurus, we hope to reduce the uncertainties in the average properties.

We determine the best model for a given spectral energy distribution by minimizing the normalized sum of the weighted squared residuals,

$$S^2 = \sum_i w_i (F_{o,i} - F_{m,i})^2 / F_{o,i} , \quad (5)$$

where $F_{o,i}$ is the observed flux at wavelength i, $F_{m,i}$ is the scaled flux of the model, and w_i is a weighting factor. The normalization of the squared residuals by $F_{o,i}$ is appropriate for errors dominated by photon statistics—which may not be correct for these sources—but this technique yields best fits that appear reasonable to the eye. Given the uncertainties in estimating observational errors and the limitations of the models, a more complicated fitting treatment is not justified.

For each source, we scaled the model fluxes to produce the correct total luminosities: $\Sigma_i F_{o,i} = \Sigma_i F_{m,i}$, where the sum is taken over all wavelengths ≥ 3.4 μm. To improve the fits, we took our standard grid of models calculated at $L = 10^{33}$, 10^{34}, and 10^{35} ergs s^{-1} and interpolated the fluxes logarithmically to produce an additional grid of models at $L = 3.16 \times 10^{33}$ ergs s^{-1} at $L = 3.16 \times 10^{34}$ ergs s^{-1}. We then scaled the model having a luminosity closest to the observed luminosity of each object. The grid only includes models for $R_c = 10$, 70, and 300 AU.

Paper II shows that scattering produces most of the near-IR emission from the Taurus-Auriga embedded sources, as expected for envelopes with bipolar holes evacuated by a molecular outflow. Our models cannot adequately calculate the near-IR emission for this geometry, so we did not include near-IR fluxes ($\lambda < 3.4$ μm) in the least-squares fit. This procedure sometimes produced a "best-fitting" model with too much near-IR emission. Because a bipolar cavity can only increase the near-IR scattering relative to our calculations, we rejected such models and chose the next-best fit.

We used weights $w_i = 1$ for wavelengths $\lambda \leq 160$ μm and chose $w_i = 0.5$ for longer wavelengths, because of the uncertainties in opacity, the difficulties in matching observational beam size with model results, and possible contributions of massive disks to the submillimeter region (cf. Beckwith et al. 1990; Butner et al. 1991; Keene & Masson 1990).

Table 2 lists the characteristics of the best-fitting models. For each source, we give the observed luminosity, the characteristic density ρ_1, the centrifugal radius R_c, and the inclination i. As shown in Figure 7, we get surprisingly good fits in many cases without including a disk, so we have not considered disks whenever possible to minimize the number of model parameters.

TABLE 2

ESTIMATED CHARACTERISTICS FOR THE EMBEDDED SOURCES

Source	log ($L/L_\odot$)	$-\log \rho_1$ (g cm^{-3})	R_c (AU)	i
04016+2610	+0.57	13.5	70	60°
04108+2803B	−0.20	13.5	70	30
04166+2706	−0.51	13.0	70	30
	...	13.5	70	90
04169+2702	−0.12	13.0	300	30
04181+2654A	−0.60	13.5	70	30
04181+2654B	−0.59	13.5	70	30–60
04181+2655	−0.42	13.0	300	30
	...	13.5	70	30
04239+2436	+0.09	13.5	70	30
04248+2612	−0.45	13.0	300	10
	...	13.5	70	30
GV Tau B	+0.77	13.5	70	30
04264+2433	−0.44	14.0	10	60
L1551 IRS 5	+1.34	12.5	300	30
	...	13.0	70	60
Haro 6-13	+0.12	14.0	70	60
04295+2251	−0.36	14.0	70	30
04302+2247	−0.48	13.0	70	60
04325+2402	−0.14	13.0	300	60
04361+2547	+0.46	13.5	10	30
04365+2535	+0.35	13.0	300	60
04368+2557	+0.13	12.5	300	60–90
04381+2540	−0.18	13.0	300	30
04489+3042	−0.53	14.0	70	30

4.1. *Comments on Individual Sources*

04016+2610.—This source lies at the western edge of an isolated NH_3 core in the L1489 dark cloud and drives a modest molecular outflow (Benson & Myers 1989; Myers et al. 1988; Terebey, Vogel, & Myers 1989; Moriarty-Schieven et al. 1992). The spectral energy distribution peaks at ~ 60 μm, which requires reasonably high densities (log $\rho_1 = -13.5$). Our best-fitting model (*dashed line*) has a significant centrifugal radius, $R_c \approx 70$ AU. ALS modeled this object with a similar infall rate, log $\rho_1 = -13.81$, but a much smaller centrifugal radius, $R_c = 9.5$ AU (see also Ladd et al. 1991a; Zinnecker et al. 1992). ALS note that their fits were judged by eye rather than by a least-squares technique. The dotted line in Figure 7 shows a model with $R_c = 10$ AU, which has larger residuals because of the much deeper silicate absorption band than in the best-fitting model. Published narrow-band observations and the good agreement between the *IRAS* 12 μm and ground-based 10 μm data suggest a weak silicate feature (Myers et al. 1987; Fig. 7), but higher accuracy 8–12 μm narrow-band photometry would provide a better constraint on the models. The object displays extended emission on optical and near-IR images and is highly polarized (Heyer et al. 1990; Tamura et al. 1991), which Paper II interprets as stellar and inner disk light scattered through a hole in the infalling envelope.

04108+2803.—The L1495 region is one of the larger dark clouds in the Taurus-Auriga complex but contains only one embedded *IRAS* source. This pair of objects consists of a heavily reddened star with near-IR colors similar to those of other T Tauri stars in the cloud (04108+2803A) and a much redder source that produces most, if not all, of the far-IR emission (04108+2803B). Neither young star shows any evidence for extended optical or near-IR emission, and there is as yet no unambiguous evidence for a molecular outflow (Tamura et al. 1991; Paper II; Terebey et al. 1989; Moriarty-Schieven et al.

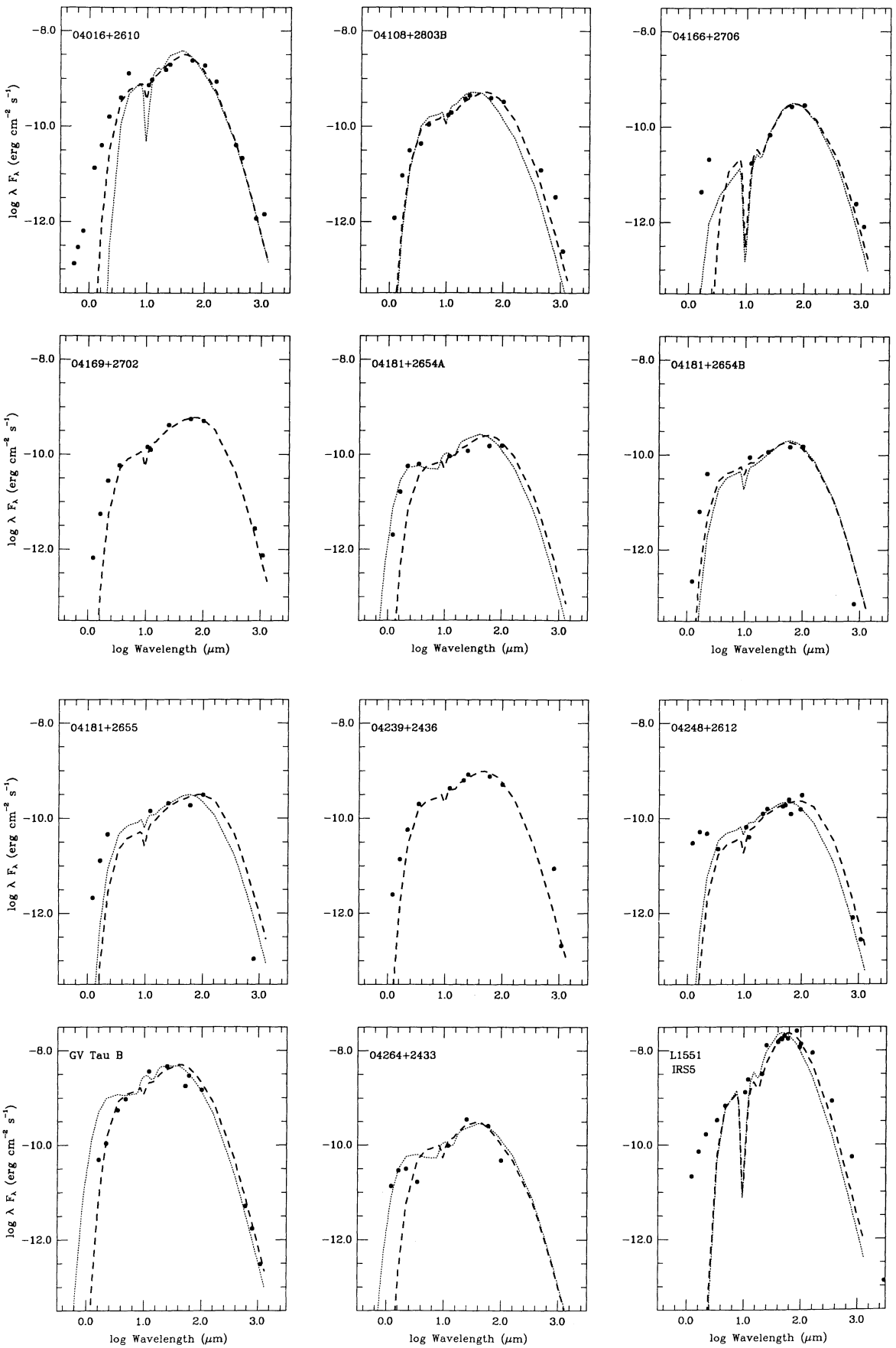

FIG. 7.—Comparison of model spectral energy distributions with observations of each embedded source. The text describes multiple curves plotted in each panel.

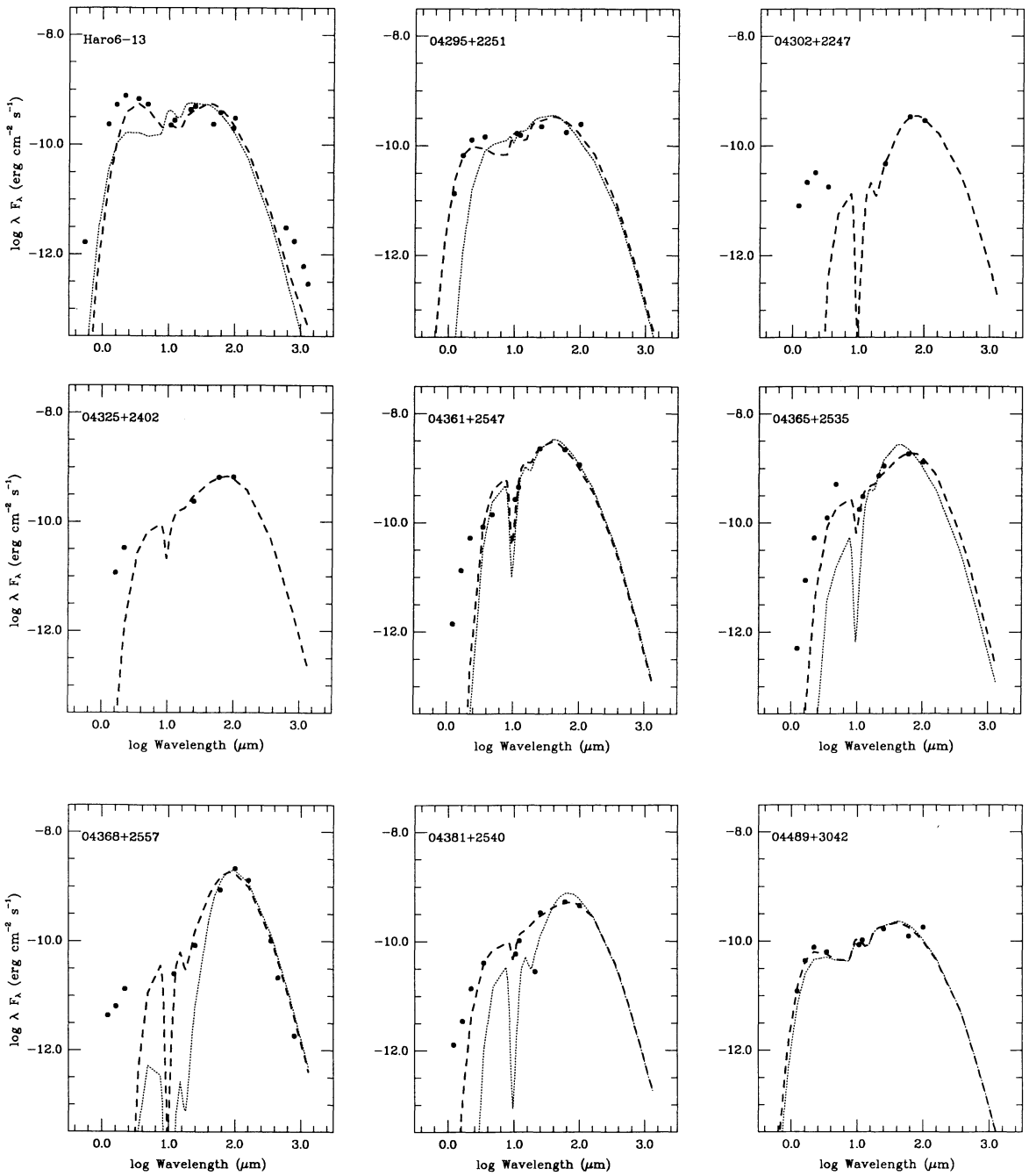

FIG. 7—*Continued*

1992). Our best-fitting model to the spectral energy distribution of 04108+2803B (*dashed line*) has a moderately large infall rate and centrifugal radius (log $\rho_1 = -13.5$; $R_c = 70$ AU). The small R_c model (log $\rho_1 = -14$, $R_c = 10$ AU; *dotted line*) fits the short-wavelength data equally well but fails to reproduce the long-wavelength fluxes. The comparison shows how several combinations of R_c and ρ_1 can produce the same optical depth in the inner envelope and thus similar spectra at short wavelengths; however, the peak of the spectral energy distribution is set by the density structure at larger radii and thus is more sensitive to ρ_1 than to R_c (in this parameter range).

04166+2706 and 04169+2702.—These two *IRAS* sources lie in a long filament (B213) that runs from the southern edge of L1495 southeast toward B217 and B218. Although the sources have similar near-IR fluxes, 04169+2702 displays a cometary nebula lying roughly parallel to the filament, while 04166+2706 appears nearly pointlike (Tamura et al. 1991; Paper II). The nebulous source, 04169+2702, also appears associated with high-velocity molecular gas (Moriarty-Schieven et al. 1992); 04166+2706 has not been observed for high-velocity gas. Ohashi et al. (1991) report a CS core near 04169+2702, but NH_3 observations of 04166+2706 and 04169+2702 have not been published.

The best-fitting model for 04166+2706 (log $\rho_1 = -13$, $R_c = 70$ AU, and $i = 30°$ [*dashed line*]) fits the long-wavelength data reasonably well. The dotted line shows a model with log $\rho_1 = -13.5$, $R_c = 70$ AU, and $i = 90°$, and demonstrates the trade-off between inclination and density. Neither model can account for the near-IR fluxes, which require substantial excess scattered light (Paper II). As we noted above, models with small R_c produce a deeper 10 μm silicate absorption feature than large-R_c models; thus additional broad-band data (L and M) and narrow-band observations across the 10 μm window for both sources would allow us to distinguish between several plausible models (see also ALS).

The peak of the spectral energy distribution of 04169+2702 indicates a relatively large density, log $\rho_1 = -13$, while the breadth of the spectral energy distribution requires $R_c \sim 300$ AU (*dashed line*).

04181+2654 and 04181+2655.—These very similar *IRAS* sources also lie in B213 but have three fairly widely separated 2 μm counterparts (Tamura et al. 1991; Paper II). Two of these objects appear nearly pointlike on near-IR images, while extended near-IR emission is clearly associated with 04181+2654B. Moriarty-Schieven et al. (1992) possibly detected high-velocity CO gas associated with 04181+2655 but did not observe 04181+2654. For simplicity, we divided the *IRAS* flux equally between the pair of 2 μm sources associated with 04181+2654 and used ADDSCAN data to divide the 100 μm flux between 04181+2654 and 04181+2655.

The minimum residual model for 04181+2654A has log $\rho_1 = -13.5$, $R_c = 70$ AU, and $i = 30°$ (*dashed line*). A lower density model (log $\rho_1 = -14$, $R_c = 70$ AU, and $i = 60°$; *dotted line*) exhibits too much near-IR flux given the probability of scattered light from an outflow cavity. The two models shown for 04181+2654B also have log $\rho_1 = -13.5$ and $R_c =$ 70 AU, and show the small difference between $i = 30°$ (*dashed line*) and $i = 60°$ (*dotted line*). Although the best-fitting model for 04181+2655 has log $\rho_1 = -13$, $R_c = 300$ AU, and $i = 30°$ (*dashed line*), the log $\rho_1 = -13.5$, $R_c = 70$ AU, and $i = 30°$ model (*dotted line*) fits better in the mid-IR. The higher density result for 04181+2655 is sensitive to the 60 and 100 μm fluxes and should be considered tentative, given the necessity of apportioning *IRAS* fluxes between two or three sources. The millimeter fluxes for both 04181+2655 and 04181+2654B lie below our model predictions, which might imply that we have overestimated the size of the emitting region. However, the three objects are not widely separated compared with the size of a typical 0.8–1 mm beam, so source confusion could produce the low 1 mm flux.

04239+2436.—This object appears to be similar to 04016+2610; it has an extended, V-shaped nebula on H and K images and a broad spectral energy distribution that peaks at 25–60 μm (Paper II; Fig. 7). Moriarty-Schieven et al. (1992) found good evidence for high-velocity molecular gas associated with this source, but it has not been mapped in NH_3 or CS. The best-fit model has a moderate infall rate, log $\rho_1 = 13.5$, and centrifugal radius $R_c = 70$ AU, with $i = 30°$ (*dashed line*). The observed 800 μm flux seems inconsistent with the other far-IR and submillimeter measurements.

04248+2612.—This young star in B217 is one of several Taurus embedded sources with a nearby Herbig-Haro object (HH 31D; HH 31 IRS 2; Cohen & Schwartz 1983; Strom et al. 1986) and lies embedded in extensive reflection nebulosity at optical and near-IR wavelengths (Strom et al. 1986; Tamura et al. 1991; Paper II). Ground-based 50–100 μm fluxes in 50″ apertures fall 50%–100% below *IRAS* measurements, so the envelope is clearly extended at far-IR wavelengths (Cohen & Schwartz 1983). The source lies $\sim 1'$ northeast of an ammonia core (Benson & Myers 1989) but does not appear associated with high-velocity molecular gas (Moriarty-Schieven et al. 1992). Our best model—log $\rho_1 = -13$, $R_c = 300$ AU, and $i = 10°$ (*dashed line*)—does not provide a much better fit to the spectral energy distribution than another model with log $\rho_1 = -13.5$, $R_c = 70$ AU, and $i = 30°$ (*dotted line*). The observed near-IR flux is very much larger than predicted by either model, which probably suggests a lower density along the rotational axis than that derived from the infall solution. In addition, the small 10 μm silicate emission feature in the data probably is not real and may be caused by the extended nature of the source.

GV Tau B.—The close pair GV Tau AB lies several arcminutes south of a dense NH_3 core in the L1524 cloud and is also associated with high-velocity moleclar gas and optical reflection nebulosity (Strom et al. 1986; Benson & Myers 1989; Terebey et al. 1989). Leinert & Haas (1989) resolved the two components using speckle interferometry; the optical source has near-IR colors similar to other T Tauri stars, while the companion has very red near-IR colors and appears to produce all of the far-IR flux. The embedded object is either extended or variable at 50–100 μm, because the flux observed in a 54″ aperture lies a factor of ~ 2 lower than the *IRAS* data (see Cohen et al. 1984). We used a 3 $L_\odot$ model to fit this 6 $L_\odot$ source, so our density may be slightly underestimated. The smallest residual model—log $\rho_1 = -14$, $R_c = 70$ AU, and $i = 60°$ (*dotted line*)—produces far too much near-IR flux, so we adopt the next best model with log $\rho_1 = -13.5$, $R_c = 70$ AU, and $i = 30°$ (*dashed line*).

04264+2433.—The embedded source is $\sim 5'$ north of the NH_3 core close to GV Tau but has not been searched for high-velocity molecular gas. Our best-fitting model—log $\rho_1 = -14$, $R_c = 10$ AU, and $i = 60°$ (*dashed line*)—requires additional scattered light to explain the near-IR fluxes. A model with the same values of ρ_1 and i but $R_c = 70$ AU (*dashed line*) produces too much flux at K and L.

L1551 IRS 5.—This classic bipolar outflow source is the most luminous embedded object in the Taurus-Auriga dark cloud and displays cometary nebulosity at optical and near-IR wavelengths (Snell, Loren, & Plambeck 1980; Strom et al. 1986; Tamura et al. 1991; Table 2). Our best fit to the spectral energy distribution has a high density, log $\rho_1 = -12.5$ for $R_c = 300$ AU and $i = 30°$ (*dashed line*), but the residuals of a log $\rho_1 = -13$ model with $R_c = 70$ AU and $i = 60°$ (*dotted line*) are not much larger.

Butner et al. (1991) described a careful study of L1551 IRS 5 and modeled both the spectral energy distribution and the spatial extent of the envelope at 50 and 100 μm. They found that these observations are consistent with a power-law density distribution $\rho \propto r^{-1.5}$ and derived a best fit for a spherically symmetric envelope model with log $\rho_1 = -2.77$. Our two best-fitting models bracket this value. Butner et al. used a minimum radius of 42 AU for their spherically symmetric dust envelope; our somewhat larger centrifugal radius estimates of 70–300 AU result in substantially larger fluxes at 4–10 μm that agree better with observations. Both our best-fitting models and the Butner et al. (G1) model predict a very deep silicate absorption feature near 10 μm, which also appears to agree with observations (Cohen & Schwartz 1983).

ALS modeled L1551 IRS 5 with log $\rho_1 = -13$ and $R_c = 43$

AU (see also Ladd et al. 1991a). They found it necessary to include radiation from a luminous disk to improve the fit in the 4–10 μm region, which we can reproduce by increasing R_c. Keene & Masson's (1990) observations require a compact source with a $\sim$45 AU radius to produce about 50% of the submillimeter flux, and this source could be a disk with a mass of $\sim 0.6\ M_\odot$. Several analyses of the optical and near-IR spectra of IRS 5 suggest that the central source is an FU Orionis object (Mundt et al. 1985; Carr, Harvey, & Lester 1987; Stocke et al. 1988); FU Orionis objects are thought to be highly luminous pre–main-sequence accretion disks (cf. Hartmann, Kenyon, & Hartigan 1993). Thus, a luminous disk should probably be included in our models and would decrease our value for R_c.

HK Tau.—We include this source in our compilation because its spectral energy distribution resembles that of GV Tau, an optical T Tauri star with an embedded companion (see above). It does not fall near an NH_3 core, nor does it appear to be associated with high-velocity molecular gas (Benson & Myers 1989; Moriarty-Schieven et al. 1992). We did not try to fit the observed spectral energy distribution, because the near-IR and mid-IR fluxes contain an unknown contribution from the optical T Tauri star. If we associate the far-IR peak with an embedded companion, then $\log \rho_1 \sim -13.5$ for $\lambda_m \sim 100$ μm using equation (4).

Haro 6-13.—The energy distribution of this source also resembles that of GV Tau. It falls $\sim 5'$ outside the contours of a dense NH_3 cloud core in TMC-2A and—like 04248+2612—does not seem associated with a dense molecular outflow (Benson & Myers 1989; Moriarty-Schieven et al. 1992). We tried to model Haro 6-13 with a luminous accretion disk viewed *through* the infalling envelope, although the possibility that it is an unresolved binary source should be considered.

Figure 7 shows two models having $\log \rho_1 = -14$, $R_c = 70$ AU; one model includes a disk with the same luminosity as the central star and has an inclination of $i = 60°$ (*dashed line*); the other model has no disk emission and is viewed at $i = 30°$ (*dotted line*).

04295+2251 and 04489+3042.—These two objects appear to be very similar. They both look pointlike at 1–2 μm, have near-IR colors comparable to the reddest optically visible T Tauri stars, and have similar, slowly rising spectral energy distributions from 2 to 100 μm (Paper II; Fig. 7). Neither source has a published ammonia map; 04295+2251 may have a molecular outflow (Moriarty-Schieven et al. 1992).

The best-fitting models for both objects have $\log \rho_1 = -14$, $R_c = 70$ AU, and $i = 30°$ (*dashed lines*). The dotted line in the panel for 04295+2251 shows a model with the same ρ_i and i but with $R_c = 10$ AU, which could be an acceptable fit if scattering through a cavity can produce additional near-IR flux. The dotted line in the panel for 04489+3042 shows the same model as the dashed line, but with an inclination of $i = 60°$ to illustrate the difficulty of inferring system inclinations.

04302+2247.—Moriarty-Schieven et al. (1992) report strong CO emission (and perhaps high-velocity gas) from this object, but it has not been mapped in a tracer of dense gas such as NH_3 or CS. Near-IR images show a monopolar morphology similar in some respects to L1551 IRS 5 (Tamura et al. 1991), so it is a good candidate for additional radio observations. The long-wavelength *IRAS* data indicate relatively high envelope densities, $\log \rho_1 = -13$; the dashed line shows a model with $R_c = 70$ AU and $i = 60°$. The near-IR fluxes are inconsistent with the high extinction of such a model and require an enhanced scattered light component, which again suggests the presence of a hole through which central radiation escapes (Paper II).

04325+2402.—This *IRAS* source in the B18 cloud drives a powerful, well-collimated monopolar molecular outflow with an estimated age of 2×10^5 yr (Heyer et al. 1987; Terebey et al. 1989). Near-IR images show an extended, bipolar nebula whose major axis lies *perpendicular* to the outflow axis, which is contrary to our expectations (Paper II). However, the outflow was mapped with a large beam on a single-dish telescope, and its orientation on small spatial scales—a few arcseconds—near the central point source is not known. The spectral observations require a dense envelope, $\log \rho_1 = -13$, and a large centrifugal radius, $R_c = 300$ AU; however, the lack of 3–10 μm data make this fit especially uncertain.

04361+2547.—In contrast to 04325+2402, this *IRAS* source in B22/HCL2 drives a well-collimated monopolar molecular outflow *along* the major axis of the extended near-IR nebula (Terebey et al. 1990; see also Tamura et al. 1991; Paper II). This region has not been mapped in NH_3; however, Terebey et al. (1990) report two peaks in ^{13}CO emission on either side of the near-IR source (see also Ohashi et al. 1991 for CS observations). A model with $\log \rho_1 = -13.5$ and $R_c = 10$ AU formally produces the best fit to the spectral energy distribution for $i = 30°$ (*dashed line*), although the $i = 60°$ model (*dotted line*) provides a better fit to the mid-IR flux. Neither model fits the data very well from 3 to 10 μm; additional *KLMN* data plus narrow-band observations across the 10 μm window would provide better tests of the models.

04365+2535.—This *IRAS* source in L1534 also lies close to the center of an NH_3 core and is associated with high-velocity molecular gas (Benson & Myers 1989; Terebey et al. 1989). The object displays weak, extended near-IR emission with (perhaps) a bipolar morphology (Tamura et al. 1991; Paper II). Our best-fitting model (*dashed line*), $\log \rho_1 = -13$, $R_c = 300$ AU, and $i = 60°$, is substantially different from the model ALS adopted ($\rho_1 = -13.66$ and $R_c = 7.4$ AU; ALS did not use a formal fitting procedure to minimize residuals). The dotted line in Figure 7 corresponds to our model with $\log \rho_1 = -13.5$ and $R_c = 10$ AU; this model does not produce enough mid-IR flux and predicts a much deeper silicate feature than observed (Myers et al. 1987). This model does not appear to agree very well with the calculation of ALS near 3 μm.

04368+2557.—This intriguing *IRAS* source lies very close to the center of an NH_3 core in the L1527 dark cloud (Benson & Myers 1989) and also appears associated with high-velocity molecular gas (Terebey et al. 1989; Moriarty-Schieven et al. 1992). Near-IR images show no evidence for a red point source near the *IRAS* position, although Tamura et al. (1991) and Paper II report an elongated ($20'' \times 40''$) patch of emission that is undoubtedly the *IRAS* source. The integrated near-IR colors for this object are very uncertain owing to its low surface brightness. We require high-density, $\log \rho_1 = -12.5$, and $R_c = 300$ AU to fit the data. Formally speaking the $i = 90°$ model (Fig. 7, *dotted line*) gives smaller residuals with our procedure because the fit is weighted by the flux, and the high inclination matches the peak of the spectral energy distribution best. However, the $i = 60°$ model (*dashed line*) provides a very much better match to the 12 and 25 μm fluxes, which are not weighted very strongly in the fit because the fluxes are so faint relative to the peak. Clearly the lower inclination model is to be preferred. Ladd et al. (1991a) inferred a comparable density, $\log \rho_1 = -12.8$, but a much smaller centrifugal radius, $R_c =$

0.04 AU, using Adams & Shu's (1986) models. The very small R_c may be inconsistent with the blue near-IR colors and extended near-IR emission observed in this source and will be explored more completely in Paper II. The Ladd et al. models also predict very deep 10 and 18 μm silicate absorption features that might be observed with narrow-band observations.

04381+2540.—This object in B14 is associated with high-velocity molecular gas but has not been mapped in detail (Terebey et al. 1989). Near-IR images show extended nebulosity with a marginally bipolar shape (Tamura et al. 1991; Paper II). We fit the spectral energy distribution of this object ignoring the 21 μm observation, which seems to be anamolously low, and need a large R_c to match the breadth of the spectral energy distribution ($\log \rho_1 = -13$, $R_c = 300$ AU, and $i = 30°$; *dashed line*). A model with $\log \rho_1 = -13$, $R_c = 70$ AU, and $i = 60°$ (*dotted line*) accounts for the 21 μm point but is much worse at all other wavelengths.

To conclude this section, we note that our infall rate estimates agree with those of ALS to factors or 2–3 for sources common to both studies. We can generally obtain "better" fits than ALS, because our approach explicitly minimizes the residuals by interpolating in a model grid. In addition, our grid has greater flexibility in fitting the data, owing to our inclusion of source inclination and luminosity as model parameters. This extra freedom leads us to infer envelope parameters that sometimes differ substantially from the ALS results, as described above. Additional observations—such as narrow-band photometry across the 10 μm window and near-IR polarization—would allow us to make more informed choices between possible model fits (see also Paper II).

5. DISCUSSION

5.1. *General Results*

The results described above and summarized in Table 2 show that the typical embedded source in Taurus can be modeled with the TSC density distribution and $\log \rho_1 \approx -13.5$. This result is relatively insensitive to values adopted for R_c and i and is probably our most robust result. Recalling equation (4), the peak wavelength of the spectral energy distribution should be proportional to $\rho_1^{1/3}$ and is only weakly dependent on source luminosity. Thus, a factor of 3 increase in density should yield a factor of 1.4 increase in the peak wavelength, which can be detected with reasonably complete photometry at 10–100 μm.

For a typical central mass of 0.5 $M_\odot$, $\log \rho_1 = -13.5$ corresponds to a mass infall rate of $\dot{M} \approx 4 \times 10^{-6}\ M_\odot\ \mathrm{yr}^{-1}$. Shu's (1977) infall theory predicts a mass infall rate of $\sim 2 \times 10^{-6}\ M_\odot\ \mathrm{yr}^{-1}$ for a wholly thermally supported cloud core with typical cloud temperature, $T = 10$ K, in Taurus (see also Stahler, Shu, & Taam 1980, 1981). We regard this as good agreement, considering the uncertainties in our calculations, dust opacities, etc. The theory also predicts an increased infall rate above the thermal values if turbulent pressure or magnetic fields or both are important in supporting cloud cores (e.g., Shu et al. 1987).

We found no acceptable fits for spherically symmetric power-law density models, because the observed spectral energy distributions are too broad at mid-IR and far-IR wavelengths. Figure 7 indicates that most sources also show extended, excess near-IR emission above levels that can be easily explained by rotating collapse models. The ubiquitous nature of this extended emission *and* high-velocity molecular gas strongly suggests that bipolar mass loss begins very early in the infall phase and carves out relatively clear lines of sight through which radiation from the central star escapes by scattering. Paper II will investigate this possibility in detail.

Our specific results for the centrifugal radii (two-thirds of the sources have $R_c \sim 70$ AU) are uncertain for several reasons. Our model grid does not have sufficient sampling in R_c, because of the extensive computation time required. Also, the spectral energy distributions show modest sensitivity to R_c in certain parameter ranges. For example, there is often little difference between the $\log \rho_1 = -13$, $R_c = 300$ AU and the $\log \rho_1 = -13.5$, $R_c = 70$ AU models, which demonstrates that the envelope density and centrifugal radius are correlated. We have neglected any contribution from a luminous disk or companion star for most objects, which could increase the near- and mid-IR fluxes by arbitrary amounts. Other sources—such as T Tau and GV Tau—are known binaries in which an optically visible star is paired with a highly reddened IR companion (e.g., Leinert & Haas 1989; Ghez et al. 1991). Some other sources in our sample—for example, HK Tau and Haro 6-13—have broad energy distributions and seem likely binaries; the interpretation of R_c for these cases is obscure.

There are also uncertainties in the dust opacity. Butner et al. (1991) point out that the Mathis, Mezger, & Panagia (1983, hereafter MMP) opacities produce a significantly flatter spectral energy distribution for L1551 IRS 5 than do the Draine & Lee (1984) opacities that we adopt. The MMP opacity law is much smaller in the mid-IR than the average interstellar reddening law (e.g., Mathis 1990); our models would thus emit more mid-IR flux if we employed MMP opacities instead of Draine & Lee (1984) opacities. Although Mathis (1990) points out some problems with producing the large, amorphous carbon grains required by Draine & Lee in the interstellar medium, Paper II shows that grain properties based on the average interstellar reddening law account for the near-IR emission in embedded sources very well. However, this potential source of uncertainty should be kept in mind when evaluating our results.

The most serious problems in our estimates for the centrifugal radius most likely arise from our neglect of strong departures from spherical symmetry in the envelope. Papers II's results show that spherically symmetric envelopes cannot explain the observed scattered-light images for most objects, and probably require more evacuated holes in the envelope than are predicted by the TSC model without bipolar flows. A rigorous temperature determination in such a geometry would probably increase the temperatures in polar directions, where radiation from the central source penetrates more easily, and decrease the temperature in equatorial regions. In addition, short-wavelength light would escape more easily through holes. Thus, we expect that models with bipolar cavities would produce a somewhat *broader* spectral energy distribution and mimic the behavior of models with large R_c. Efstathiou & Rowan-Robinson's (1990) more detailed radiative transfer calculations showed that the ratio of the polar axis temperature to the temperature in the equatorial plane at the same radius was always between ~ 1.10 and 1.25 for some TSC models, but the inclusion of a truly evacuated hole probably would make much larger changes in the temperature distribution.

The inclinations derived are very uncertain. The spectral energy distribution models indicate $i \lesssim 30°$ for roughly half of the sources, while the scattering models point to source inclinations closer to $i = 60°$–$90°$ (Paper II). Higher inclination

models for the spectral energy distributions require larger R_c to produce an equal amount of mid-IR flux. Again, the limited number of models in our grid may be responsible for this behavior. As we note in Paper II, detailed mapping of the bipolar outflows and imaging polarimetry of the near-IR emission would give us a better idea of individual source inclinations for comparison with the models.

In summary, we believe estimates for the envelope densities, which constrain infall rates, to be our most conclusive result. The R_c estimates are more suggestive than conclusive, although for many objects the models suggest R_c values consistent with Paper II. The R_c estimates also compare rather well with outer disk radii estimated for many T Tauri stars (e.g., Beckwith et al. 1990); however, these revealed sources are much older than the embedded objects, and their disks may have expanded significantly from viscous evolution. Aside from L1551 IRS 5, we have very little independent information for source inclination angles and must wait for additional data before we can constrain this parameter of our models.

5.2. *The Luminosity Problem*

Both Myers et al. (1987) and Kenyon et al. (1990) estimated the characteristic age of a Taurus-Auriga embedded source to be ~ 1–2×10^5 yr, based on the relative numbers of embedded sources and T Tauri stars (TTS) in the cloud and the apparent age, $\sim 10^6$ yr, for an optically visible TTS. If an embedded source accretes $\sim 0.5\ M_\odot$ to form a typical TTS during this time, then the time-averaged accretion rate must be $\dot{M} \sim 2.5$–$5 \times 10^{-6}\ M_\odot\ \mathrm{yr}^{-1}$, which is close to the expected infall rate for most cloud cores in Taurus-Auriga (ALS). Our results for the envelope density provide an independent constraint on the mass infall rate of the envelope, and our estimate of $\dot{M} \sim 4 \times 10^{-6}\ M_\odot\ \mathrm{yr}^{-1}$ agrees with the rate required from source statistics. Thus, our median $\log \rho_1 = -13.5$ produces a representative TTS with mass $\sim 0.5\ M_\odot$ in ~ 1–2×10^5 yr, which is consistent with the relative numbers of embedded and optically visible pre–main-sequence stars in Taurus-Auriga.

However, Kenyon et al. (1990; see also Adams & Shu 1986) pointed out that the embedded source luminosities are roughly an order of magnitude smaller than expected if material falls to the radius of a typical TTS at the measured infall rate. The accretion luminosity is simply $L = GM_* \dot{M}_i / R_*$, which can be written as

$$L \approx 5\ L_\odot \left(\frac{\dot{M}_i}{10^{-6}\ M_\odot\ \mathrm{yr}^{-1}}\right)\left(\frac{M_*}{0.5\ M_\odot}\right)\left(\frac{R_*}{3\ R_\odot}\right)^{-1} . \quad (6)$$

Kenyon et al. estimated that the median luminosity of $\sim 1\ L_\odot$ implied an accretion rate comparable to that of optically visible T Tauri stars, $\dot{M} \sim 1$–$2 \times 10^{-7}\ M_\odot\ \mathrm{yr}^{-1}$, for a typical mass, $M_* \sim 0.5\ M_\odot$, and radius $R_* \sim 2$–$3\ R_\odot$. This accretion rate is obviously inconsistent with the infall rates derived above. Kenyon et al. extended this analysis to a simple model for a population of accreting protostars of varying masses and again found an order-of-magnitude discrepancy between the observed and predicted median luminosities.

Kenyon et al. (1990) discussed several ways to reduce the luminosity problem. A straightforward solution simply assumes that we have somehow underestimated the ages of optically visible TTS. Kenyon et al. based their infall rates on relative source statistics, so an increase in the typical ages of TTS would similarly increase the lifetime of the embedded phase and consequently decrease the infall rate for the embedded objects. Our radiative transfer models provide an independent, albeit indirect, constraint on the infall rates. We find median infall rates comparable to those estimated by Kenyon et al. and other investigators (and also with theoretical estimates); thus, the luminosity problem cannot be solved in this way. As a by-product of this analysis, our results also indicate that the TTS ages have not been significantly underestimated given current source statistics.

Another "obvious" explanation of the luminosity problem allows material to fall onto a disk, and produce a lower accretion luminosity (see eq. [6]), instead of falling directly onto the central star. Our large R_c estimates support this solution. However, material must still somehow flow from the disk to the star at some point in the pre–main-sequence phase, so this resolution of the luminosity problem is not sufficient by itself. We believe that young stars do not accrete most of their final mass during the optically visible T Tauri phase, given current estimates for ages and accretion rates (Hartmann & Kenyon 1990). Moreover, recent theoretical calculations suggest that no more than one-quarter of the total system mass can reside in the disk; otherwise gravitational instabilities develop and transfer angular momentum outward and mass inward on very rapid time scales (Adams, Ruden, & Shu 1989; Shu et al. 1990). Thus, most of the system mass probably cannot reside in the disk for any appreciable length of time.

Our infall rate estimates, combined with the observed low source luminosities reinforce the suggestion that FU Orionis outbursts resolve the luminosity problem (Kenyon et al. 1990). In this picture, an infalling envelope adds mass to a disk at a rate $\sim 4 \times 10^{-6}\ M_\odot\ \mathrm{yr}^{-1}$, while the disk accretion rate onto the star is closer to $\dot{M} \sim 1$–$2 \times 10^{-7}\ M_\odot\ \mathrm{yr}^{-1}$. Material then piles up in the disk until it becomes unstable (gravitationally or otherwise) and the accretion rate increases dramatically. The peak accretion rate in typical FU Orionis eruptions is $\sim 10^{-4}\ M_\odot\ \mathrm{yr}^{-1}$ (Hartmann et al. 1993); this high accretion rate reduces the disk mass on a short time scale and the disk eventually becomes stable again and returns to its low accretion rate state. The luminosity function of a population of embedded sources would then have a low-luminosity peak corresponding to the low accretion rate characteristic of most of the evolution, with a few high-luminosity objects in the outburst (high) state. If we assume that a TTS accumulates a typical mass of $0.5\ M_\odot$ in bursts of high accretion rate, $\dot{M} \sim 10^{-4}\ M_\odot\ \mathrm{yr}^{-1}$, during the $\sim 10^5$ yr lifetime of a typical embedded source, then we would expect approximately 5% of the embedded sources to be in the outburst state. In our Taurus population of ~ 20 embedded sources, we would therefore expect to see ~ 1 FU Orionis variable. The identification of L1551 IRS 5 as an FU Orionis variable (albeit with an order of magnitude lower luminosity than is typical) is clearly consistent with these crude statistics.

5.3. *Source Ages and Evolution*

We now look at the problems of source luminosity, age, and evolution in more detail, and assume that the inside-out, isothermal TSC collapse model is correct. In this model, the mass infall rate is a constant,

$$\dot{M}_i = 0.975 a^3 / G , \quad (7)$$

where a is the sound speed in the originally thermally supported cloud. Thus, the stellar core mass, M_*, increases linearly with time since the beginning of the collapse, $M_* = \dot{M}_i t$. The density normalization $\rho_1 \propto M_*^{-1/2} \propto t^{-1/2}$ can be found

from equation (3). Transforming the results of TSC into convenient units, we have

$$R_c = 0.24\Omega_{-14}^2 a_{0.2} t_5^3 \text{ AU} , \quad (8)$$

where Ω_{-14} is the angular velocity of the initial uniformly rotating cloud in units of 10^{-14} s^{-1}, $a_{0.2}$ is the sound speed in units of 0.2 km s^{-1} (corresponding to $T = 10$ K), and t_5 is the age in units of 10^5 yr.

We can complete the characterization of the model with a prescription for the central luminosity. In steady state, the accretion luminosity would be given by equation (6), which neglects any additional luminosity from gravitational contraction in the stellar interior. As discussed above, the accretion rate onto the central source seems to be much less than the infall rate [at least the central luminosity is less than that given by equation (6)]. We therefore assume $\dot{M}_{\rm acc} = \alpha \dot{M}_i$, where $\alpha \leq 1$; then

$$L = GM_* \dot{M}_{\rm acc}/R_* . \quad (9)$$

We assume that the central core has a radius on the stellar "birth line" for a given mass, namely, $R_* \approx 4.8(M_*/M_\odot)^{0.6} R_\odot$ for $M_* \geq 0.3 M_\odot$, and $R_* \approx 2.5 R_\odot$ for $M_* < 0.3 M_\odot$ (Stahler 1988).

Figure 8 (*top panel*) shows evolutionary tracks calculated in this way for $\alpha = 1$; we also include our estimates for the Taurus-Auriga embedded sources. The evolutionary tracks for a given initial sound speed are labeled by the logarithm of the (constant) mass infall rate in solar masses per year. The nearly horizontal solid lines are isochrones, labeled by the logarithm of the age in years. The dashed and dotted lines denote positions where $R_c = 70$ AU for $\Omega = 10^{-13}$ s^{-1} and $\Omega = 10^{-14}$ s^{-1}, respectively.

Apart from the highest luminosity source, L1551 IRS 5, and 04368+2557, most of the embedded sources cluster in a range of one order of magnitude in luminosity and in ρ_1. The upper panel of Figure 8 indicates a mean age of $\sim 3 \times 10^4$ while the majority of sources have ages less than 10^5 yr. These time scales are uncomfortably small given the source statistics (see above; Kenyon et al. 1990). In effect, this model "solves" the luminosity problem by making the central mass $\sim 0.1 M_\odot$. This mass is considerably smaller than the mass of a typical T Tauri star, and it seems very unlikely that the majority of the embedded sources have such small masses. Furthermore, our estimated centrifugal radii of 70–300 AU are much larger than can be produced in these times scales with the maximum angular velocities, $\Omega = 10^{-13}$ s^{-1}, indicated by observations of molecular cloud cores (TSC; Arquilla & Goldsmith 1985, 1986; Goodman et al. 1993).

Following the discussion of the previous section, we consider results for $\alpha = 0.1$ in Figure 8 (*lower panel*). The median embedded source age, $\sim 1 \times 10^5$ yr, then agrees with the age estimated from source statistics, and the typical mass, $\sim 4 \times 10^{-6} M_\odot$ yr$^{-1} \times 10^5$ yr $\sim 0.4 M_\odot$, also seems more plausible. Furthermore, the largest observed cloud angular velocities can produce $R_c \sim 70$ AU for the average source on this time scale. We conclude that the TSC model for source evolution is more consistent with $\alpha = 0.1$ than with $\alpha = 1$.

The models predict a general decrease in ρ_1 as a function of time, because the mass increases with time and $\rho_1 \propto M_*^{-1/2}$. However, the scatter in the lower panel of Figure 8 is not consistent with source evolution for two reasons. First, we expect more older sources for the roughly continuous birthrate over 10^5 yr, but we see no evidence for this behavior. Second,

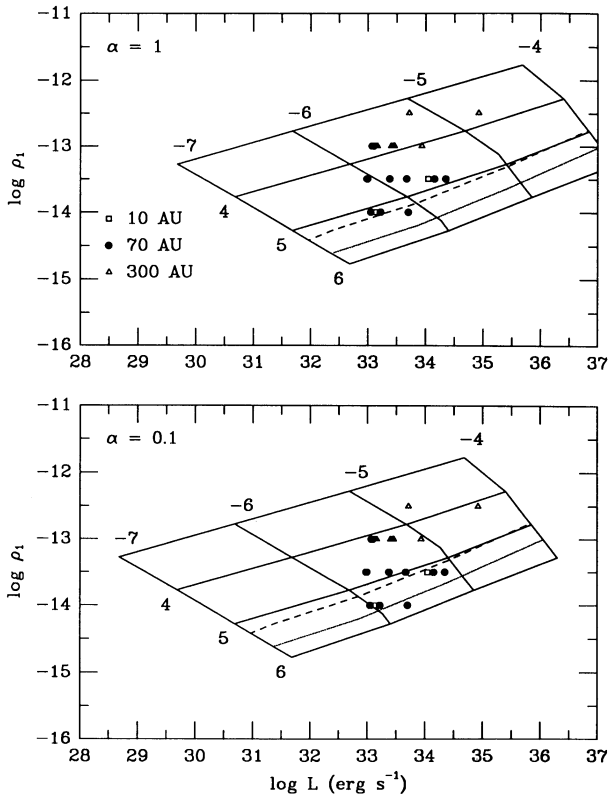

FIG 8.—Model results in the (log ρ_1, log L)-plane compared with evolutionary properties predicted by the TSC rotating collapse model (see text). The source properties are taken from best-fitting models in Table 5; open squares, filled circles, and open triangles correspond to $R_c = 10$, 70, and 300 AU, respectively. The curves sloping from upper right to lower left correspond to evolution in the TSC model for four differing infall rates, $\dot{M} = 10^{-7}$, 10^{-6}, 10^{-5}, and $10^{-4} M_\odot$ yr^{-1}, respectively, with labels corresponding to the exponent. The nearly horizontal solid lines are isochrones, labeled by the logarithm of the age in years. The dashed and dotted lines denote positions where $R_c = 70$ AU for $\Omega = 10^{-13}$ and 10^{-14} s^{-1}, respectively *Top*: model tracks calculated for the same accretion rate onto the star as onto the disk ($\alpha = 1$; see text). *Bottom*: same as above, but for $\alpha = 0.1$.

the sources with the largest ρ_1 should have the smallest R_c (because $R_c \propto t^3$), but the Taurus-Auriga sources display the opposite relation. In addition, the scaling of R_c with age suggests that our sample should contain a substantial number with small R_c; however, none of these objects can be fitted with a spherically symmetric model as described above.

In the previous section, we noted some effects that might lead us to overestimate R_c and could account for the apparent absence of small-R_c objects. Aside from these possibilities, some physical process other than rotation might produce flattened dusty envelopes. Galli & Shu (1993a, b; see also Mouschovias & Morton 1991, 1992) suggest the magnetic field threading a protostellar cloud could significantly retard collapse in the equatorial regions and lead to a flattened density distribution for the collapsing cloud. Radiative transfer calculations in the non–spherically symmetric geometry are needed to explore the application of this model to embedded sources.

There might also be an observational selection effect that accounts for the apparent absence of small-R_c objects. The TSC model predicts that the smallest R_c objects will be the youngest and hence will have the lowest luminosities. Small-R_c low L sources will be very red and therefore very difficult to

detect, because we need to observe them at wavelengths shorter than 60 μm to be sure of source identification. If we scale from the coldest embedded sources in the sample, the typical detection limit of $F_\nu \sim 0.25$ Jy at 25 μm corresponds to a minimum detectable luminosity of $\sim 0.2\ L_\odot$. The luminosity of our faintest source is $\sim 0.25\ L_\odot$, so very young, small-R_c objects may yet be found in Taurus.

The apparent absence of older sources may be another selection effect. Our low-density models show that substantial amounts of near-IR light can escape from the envelope for the large centrifugal radii expected at late times in the infall. Indeed, "old" infall models can even produce detectable amounts of optical light, especially if the envelope contains a bipolar cavity. Thus, we suggest that the missing older sources—with low-density envelopes and large R_c—have been identified as T Tauri stars with large IR excesses.

6. SUMMARY

We have described radiative transfer calculations for the spectral energy distributions of a complete sample of deeply embedded young stars in the Taurus-Auriga molecular cloud. If the dusty envelopes surrounding these objects are collapsing, we estimate a typical infall rate of $\sim 4 \times 10^{-6}\ M_\odot\ \mathrm{yr}^{-1}$, which agrees well with theoretical predictions (e.g., Shu 1977; TSC; ALS) and with observed source statistics. We also find that the dusty envelopes cannot be spherically symmetric. Our model results seem consistent with rotational flattening for a centrifugal radius of ~ 100 AU (TSC). Various estimates suggests disks with similar radii in optically visible T Tauri stars, so rotational infall appears to be a reasonable mechanism for disk production in young stars. In addition, the bolometric luminosities of these young stars fall an order of magnitude lower than expected for the observed infall rate if material flows directly to a characteristic stellar radius of a few $R_\odot$. This result provides independent evidence that cloud material falls into a circumstellar disk instead of the central star. Many embedded sources also display considerable excess near-IR emission over that predicted by our transfer calculations. Scattering of stellar and inner disk radiation through a wind-blown cavity may account for the excess emission and will be discussed further in Paper II.

We acknowledge R. Hewett for assistance with collecting the infrared observations reported in this paper. We also thank B. Whitney for constructive comments and the referee, F. Shu, for suggestions that improved our presentation. This research was supported by the Scholarly Studies Program and the International Exchange Program of the Smithsonian Institution, and by the National Aeronautics and Space Administration through grant NAGW-2306.

APPENDIX

We derive approximate relations for the temperature distribution in the envelope following Larson's (1972) original analysis. At large radial distances, the envelope is optically thin to its (low-temperature) radiation. The radiative equilibrium equation

$$\int \kappa_\nu (J_\nu - B_\nu) d\nu = 0 \tag{A1}$$

simplifies at small optical depth in the spherical atmosphere, where the opacity has no temperature dependence and $\int \kappa_\nu J_\nu d\nu \rightarrow$ constant $\times\ r^{-2}$. Larson (1972) showed that the Planck mean opacity varies as $\kappa_P \propto T^p$ for $\kappa_\lambda \propto \lambda^{-p}$, so the temperature becomes

$$T(r) \propto r^{-2/(4+p)}\ . \tag{A2}$$

This equation implies $T \propto r^{-1/3}$ for $p = 2$, which is characteristic of our adopted far-IR opacity law (Draine & Lee 1984).

We can derive simple relations for the temperature gradient and the peak wavelength of the spectral energy distribution in the limit of large optical depths with the standard diffusion approximation

$$L = -\frac{64\pi\sigma r^2 T^3}{3\kappa_R \rho}\frac{dT}{dr}\ , \tag{A3}$$

where κ_R is the Rosseland mean opacity. Again, we have $\kappa_R \propto T^p$ for a power-law dependence of opacity, $\kappa_\lambda \propto \lambda^{-p}$. The mass density also depends primarily on radius in TSC's picture, so we can write $\rho = \rho_0 (r/r_0)^{-n}$ and integrate equation (A3) with the boundary condition that $T \rightarrow 0$ as $r \rightarrow \infty$, to get

$$T \propto (L\rho_0 r_0^n)^{1/(4-p)} r^{-(1+n)/(4-p)}\ . \tag{A4}$$

The temperature ranges from ~ 1500 K at the dust destruction radius to ~ 100 K near the outer edge of the optically thick region, so most of the radiation has $\lambda \sim 3$–30 μm. The opacity is hardly a simple power-law function of wavelength in this domain, which limits the applicability of this analysis. Even so, the Rosseland mean opacity scales very roughly with temperature as $T^{1/2}$ between ~ 100 and 1000 K for Draine & Lee (1984) grains, which yields a temperature relation in approximate agreement with the models for $n = 3/2$:

$$T \propto (L\rho_0 r_0^{3/2})^{2/7} r^{-5/7}\ . \tag{A5}$$

The diffusion approximation for a power-law opacity implies that the radius r at which a given constant temperature T occurs scales as $r \propto (L\rho_1)^{1/(1+n)}$. The variation of the dust destruction radius ($T \approx 1500$ K) among the models is roughly consistent with the expected scaling, $r \propto (L\rho_1)^{2/5}$, for $n = 3/2$.

To further investigate the scaling of the models, we crudely approximate the emergent protostar spectrum as a blackbody with the peak flux at a wavelength λ_m. The dust envelope then has a characteristic effective temperature $T_m = 0.3/\lambda_m$, and the emitted luminosity is

$$L = 4\pi r_{\lambda_m}^2 \sigma T_m^4 , \tag{A6}$$

where r_{λ_m} is the radius at which $T(\lambda_m)$ occurs. If we further assume that r_{λ_m} is the "photospheric" radius where the radial optical depth is $\tau_{\lambda_m} = \frac{2}{3}$, we can solve for λ_m, $T(\lambda_m)$, and r_{λ_m} for a given optical distribution and total luminosity.

If cloud material collapses at the free-fall velocity, the radial optical depth through an envelope with a very large outer radius is

$$\tau_\lambda = \frac{\kappa_\lambda \dot{M}}{2\pi(2GM)^{1/2}} r^{-1/2} . \tag{A7}$$

The photospheric radius is then

$$r_\lambda = \frac{9}{4} \frac{\kappa_\lambda^2 \dot{M}^2}{8\pi G M_*} . \tag{A8}$$

If we approximate the opacity as $\kappa_\lambda = \kappa_0(\lambda/\lambda_0)^{-p}$, we can substitute

$$\frac{\lambda}{\lambda_0} = \left(\frac{0.3}{\lambda_0}\right)^{1/(1+p)} \left(\frac{4\pi\sigma}{L}\right)^{1/(4+4p)} \left(\frac{9\dot{M}^2\kappa_0^2}{32\pi G M_*}\right)^{1/(2+2p)} . \tag{A9}$$

If we take the far-IR opacity to be $\kappa_\lambda = 0.2(\lambda/100\ \mu\text{m})^{-2}$, and recast this result in terms of $\rho_1 \propto \dot{M} M_*^{-1/2}$,

$$\lambda_m = 60 L_{33}^{-1/12} \rho_{1,13}^{1/3}\ \mu\text{m} , \tag{A10}$$

where L_{33} is the luminosity in units of 10^{33} ergs cm^{-2} s^{-1} and $\rho_{1,13}$ is the density at 1 AU in units of 10^{-13} g cm^{-3}. The corresponding "effective temperature" of the dusty envelope, T_m, which roughly marks the transition between optically thin and optically thick regimes, is

$$T_m = 50 L_{33}^{1/12} \rho_{1,13}^{-1/3}\ \text{K} . \tag{A11}$$

For $L_{33} = 1 = \rho_{1,13}$, Figure 1 shows that the radial temperature distribution does indeed change from the optically thick limit to the optically thin limit near 50 K. The analytic scaling of the temperature as a function of the luminosity and density also agrees reasonably well with the model results. The "photospheric radius" should scale as $L^{1/3}\rho_1^{2/3}$. These scaling laws begin to break down for $\rho_1 = 10^{-14}$ g cm^{-3}, because the relevant opacity is then in the 30 μm region, where the λ^{-2} scaling of the opacity is no longer a good approximation.

REFERENCES

Adams, F. C., & Shu, F. H. 1985, ApJ, 296, 655
Adams, F. C., Emerson, J. P., & Fuller, G. A. 1990, ApJ, 357, 606
Adams, F. C., Lada, C. J., & Shu, F. H. 1987, ApJ, 312, 788 (ALS)
Adams, F. C., Ruden, S. P., & Shu, F. H. 1989, ApJ, 358, 495
Adams, F. C., & Shu, F. H. 1986, ApJ, 308, 836
Arquilla, R., & Goldsmith, P. F. 1985, ApJ, 297, 436
———. 1986, ApJ, 303, 356
Barsony, M., & Kenyon, S. J. 1992, ApJ, 384, L53
Beckwith, S. V. W., & Sargent, A. I. 1991, ApJ, 381, 250
Beckwith, S. V. W., Sargent, A. I., Chini, R. S., & Güsten, R. 1990, AJ, 99, 924
Beichman, C. A., Boulanger, F., & Moshir, M. 1992, ApJ, 386, 248
Beichman, C., & Harris, S. 1981, ApJ, 245, 589
Beichman, C. A., Myers, P. C., Emerson, J. P., Harris, S., Mathieu, R., Benson, P. J., & Jennings, R. E. 1986, ApJ, 307, 337
Benson, P. J., & Myers, P. C. 1989, ApJS, 71, 89
Benson, P. J., Myers, P. C., & Wright, E. L. 1984, ApJ, 279, L27
Bessell, M. S., & Brett, J. M. 1988, PASP, 100, 1134
Butner, H. M., Evans, N. J., II, Lester, D. F., Levereault, R. M., & Strom, S. E. 1991, ApJ, 376, 636
Carr, J. S., Harvey, P. M., & Lester, J. S. 1987, ApJ, 321, L71
Cassen, P., & Moosman, A. 1981, Icarus, 48, 353
Cassinelli, J. P., & Hartmann, L. W. 1975, ApJ, 202, 718
Cassinelli, J. P., & Hummer, D. G. 1971, MNRAS, 153, 9
Chini, P., Kreysa, E., Mezger, P. G., & Gemund, H.-P. 1984, A&A, 137, 117
Cohen, M., Harvey, P. M., & Schwartz, R. D. 1985, ApJ, 296, 633
Cohen, M., & Kuhi, L. V. 1979, ApJS, 41, 743
Cohen, M., & Schwartz, R. D. 1983, ApJ, 265, 877
Cohen, H., Schwartz, R. D., Harvey, P. M., & Wilking, B. A. 1984, ApJ, 278, 671
Draine, B. T. 1987, Princeton Obs. preprint, No. 213
Draine, B. T., & Lee, H. M. 1984, ApJ, 285, 89
Efstathiou, A., & Rowan-Robinson, M. 1990, MNRAS, 245, 275
Elias, J. H. 1978, ApJ, 224, 857
Emerson, J. P. 1988, in Formation and Evolution of Low Mass Stars, ed. A. K. Dupree & M. V. T. V. Lago (Dordrecht: Kluwer), 193
Galli, D., & Shu, F. H. 1993a, ApJ, submitted
Galli, D., & Shu, F. H. 1993b, ApJ, submitted
Ghez, A., Neugebauer, G., Gorham, P. W., Haniff, C. A., Kulkarni, S. R., Matthews, K., Koresko, C., & Beckwith, S. 1991, AJ, 102, 2066
Goodman, A. A., Benson, P. J., Fuller, G. A., & Myers, P. C. 1993, ApJ, 406, 528
Hartmann, L. W., & Kenyon, S. J. 1990, ApJ, 349, 190
Hartmann, L. W., Kenyon, S. J., & Hartigan, P. 1993, in Protostars and Planets III, ed. E. H. Levy, & M. S. Mathews, in press
Harvey, P. M., Thronson, H. A., Jr., & Gatley, I. 1979, ApJ, 231, 115
Heyer, M. H., Ladd, E. F., Myers, P. C., & Campbell, B. 1990, AJ, 99, 1585
Heyer, M. H., Snell, R. L., Goldsmith, P. F., & Myers, P. C. 1987, ApJ, 321, 370
Hummer, D. G., & Rybicki, G. B. 1971, MNRAS, 152, 1
IRAS Point Source Catalog, Version 2. 1988, Joint *IRAS* Science Working Group (Washington, DC: GPO)
Keene, J., & Masson, C. R. 1990, ApJ, 355, 635
Kenyon, S. J., & Hartmann, L. W. 1993, in preparation
Kenyon, S. J., Hartmann, L. W., Strom, K. M., & Strom, S. E. 1990, AJ, 99, 869
Kenyon, S. J., Whitney, B., Gomez, M., & Hartmann, L. 1993, ApJ, 414, 773 (Paper II)
Kim, C. Y. 1990, Mem. Fac. Sci. Kyto. Univ. Ser. Phys. Astron. Geophys. & Chem., 38, 1
Kleinmann, S. G., Cutri, R. M., Young, E. T., Low, F. J., & Gillett, F. C. 1986, Explanatory Supplement to the *IRAS* Serendipitous Survey Catalog (Pasadena: JPL)
Ladd, E. F., Adams, F. C., Casey, S., Davidson, J. A., Fuller, G. A., Harper, D. A., Myers, P. C., & Padman, R. 1991a, ApJ, 366, 203
———. 1991b, ApJ, 382, 555
Larson, R. B. 1972, MNRAS, 157, 121
Leinert, Ch., & Haas, M. 1989, A&A, 222, 110
Mathis, J. S. 1990, ARA&A, 28, 37
Mathis, J. S., Mezger, P., & Panagia, N. 1983, A&A, 128, 212
Mihalas, D. 1978, Stellar Atmospheres (San Francisco: Freeman)
Moneti, A., & Zinnecker, H. 1991, A&A, 242, 428
Moriarty-Schieven, G. H., Wannier, P. G., Tamura, M., & Keene, J. B. 1992, ApJ, 400, 260
Mouschovias, T. Ch., & Morton, S. A. 1991, ApJ, 371, 296

Mouschovias, T. Ch., & Morton, S. A. 1992, ApJ, 390, 166
Mundt, R., Stocke, J., Strom, S. E., Strom, K. M., & Anderson, E. R. 1985, ApJ, 297, L41
Myers, P. C., Fuller, G. A., Mathieu, R. D., Beichman, C. A., Benson, P. J., Schild, R. E., & Emerson, J. P. 1987, ApJ, 319, 340
Myers, P. C., Heyer, M., Snell, R. L., & Goldsmith, P. F. 1988, ApJ, 324, 907
Ohashi, N., Kawabe, R., Hayashi, M., & Ishiguro, M. 1991, AJ, 102, 2054
Price, S. D., & Murdock, T. L. 1983, AFGL-TR-83-0161
Price, S. D., Murdock, T. L., & Shivanandan, K. AFGL-TR-83-0055
Rieke, G. H., Lebofsky, M. J., & Low F. J. 1985, AJ, 90, 900
Rydgren, A. E., & Vrba, F. J. 1983, AJ, 88, 1017
Shu, F. H. 1977, ApJ, 214, 488
Shu, F. H., Adams, F. C., & Lizano, S. 1987, ARA&A, 25, 23
Shu, F. H., Tremaine, S., Adams, F. C., & Ruden, S. P. 1990, ApJ, 358, 495
Snell, R. L., Loren, R. B., & Plambeck, R. L. 1980, ApJ, 286, 529
Stahler, S. W. 1988, ApJ, 332, 804
Stahler, S. W., Shu, F. H., & Taam, R. E. 1980, ApJ, 241, 637
———. 1981, ApJ, 248, 797
Stocke, J. T., Hartigan, P. M., Strom, S. E., Strom, K. M., Anderson, E. R., Hartmann, L. W., & Kenyon, S. J. 1988, ApJS, 68, 229
Strom, K. M., Strom, S. E., Edwards, S., Cabrit, S., & Skrutskie, M. F. 1989, AJ, 97, 1451
Strom, K. M., Strom, S. E., & Vrba, F. J. 1976, AJ, 81, 320
Strom, K. M., Strom, S. E., Wolf, S. C., Morgan, J., & Wenz, M. 1986, ApJS, 62, 39
Tamura, M., Gatley, I., Waller, W., & Werner, M. W. 1991, ApJ, 374, L25
Tamura, M., & Sato, S. 1989, AJ, 98, 1368
Terebey, S., Beichman, C. A., Gautier, T. N., & Hester, J. J. 1990, ApJ, 362, L63
Terebey, S., Shu, F. H., & Cassen, P. 1984, 286, 529
Terebey, S., Vogel, S. N., & Meyers, P. C. 1989, ApJ, 340, 472
Ulrich, R. K. 1976, ApJ, 210, 377
Weaver, W. B., & Jones, G. 1992, ApJS, 78, 239
Weintraub, D. A., Sandell, G., & Duncan, W. D. 1989, ApJ, 340, L69
Wilking, B. A., Lada, C. J., & Young, E. T. 1989, ApJ, 340, 823
Wolfire, M. G., & Cassinelli, J. P. 1987, ApJ, 319, 850
Zinnecker, H., Bastien, P., Arcoragi, J.-P., & Yorke, H. W. 1992, A&A, 265, 726